1   **Earth Observations from DSCOVR/EPIC Instrument**

2   Alexander Marshak (NASA/GSFC; alexander.marshak@nasa.gov),
3   Jay Herman (UMBC; jay.r.herman@nasa.gov),
4   Adam Szabo (NASA/GSFC; adam.szabo-1@nasa.gov),
5   Karin Blank (NASA/GSFC; karin.b.blank@nasa.gov),
6   Alexander Cede (GESTAR; alexander.cede@nasa.gov),
7   Simon Carn (Michigan Technological University; scarn@mtu.edu),
8   Igor Geogdzhayev (Columbia University; igor.v.geogdzhayev@nasa.gov),
9   Dong Huang (SSAI; dong.huang@nasa.gov),
10   Liang-Kang Huang (SSAI; liang-kang.huang@ssaihq.com),
11   Yuri Knyazikhin (Boston University; jknjazi@bu.edu),
12   Matthew Kowalewski (USRA; matthew.g.kowalewski@nasa.gov),
13   Nickolay Krotkov (NASA/GSFC; nickolay.a.krotkov@nasa.gov),
14   Alexei Lyapustin (NASA/GSFC; alexei.i.lyapustin@nasa.gov),
15   Richard McPeters (NASA/GSFC; richard.d.mcpeters@nasa.gov),
16   Omar Torres (NASA/GSFC; omar.o.torres@nasa.gov),
17   Yuekui Yang (NASA/GSFC; yuekui.yang-1@nasa.gov)
18
19
20   Corresponding author: Alexander Marshak
21   NASA - Goddard Space Flight Center
22   NASA/GSFC (Code 613), Greenbelt MD 20771
23   E-mail: Alexander.Marshak@nasa.gov
24

25   **Abstract**

26   The NOAA Deep Space Climate Observatory (DSCOVR) spacecraft was launched on

27   February 11, 2015, and in June 2015 achieved its orbit at the first Lagrange point or L1,

28   1.5 million km from Earth towards the Sun. There are two NASA Earth observing

29   instruments onboard: the Earth Polychromatic Imaging Camera (EPIC) and the National

30   Institute of Standards and Technology Advanced Radiometer (NISTAR). The purpose of

31   this paper is to describe various capabilities of the DSCOVR/EPIC instrument. EPIC

32   views the entire sunlit Earth from sunrise to sunset at the backscattering direction

33   (scattering angles between 168.5° and 175.5°) with 10 narrowband filters: 317, 325, 340,

34   388, 443, 552, 680, 688, 764 and 779 nm. We discuss a number of pre-processing

35   steps necessary for EPIC calibration including the geolocation algorithm and the

36   radiometric calibration for each wavelength channel in terms of EPIC counts/second for

37   conversion to reflectance units. The principal EPIC products are total ozone O_3

38   amount, scene reflectivity, erythemal irradiance, UV aerosol properties, sulfur dioxide

39   SO_2 for volcanic eruptions, surface spectral reflectance, vegetation properties, and cloud

40   products including cloud height. Finally, we describe the observation of horizontally

41   oriented ice crystals in clouds and the unexpected use of the O2 B-band absorption for

42   vegetation properties.

43

44   **Capsule Summary**

45   The Earth Polychromatic Imaging Camera (EPIC) on board DSCOVR spacecraft is

46   located at 1 million miles from Earth towards the Sun. This paper describes EPIC

47   calibration and products.

1. Introduction

The Deep Space Climate Observatory (DSCOVR) was launched on February 11, 2015 to a Sun-Earth Lagrange-1 (L1) orbit, approximately 1.5 million kilometers from Earth towards the Sun. Its mission is to provide continuous solar wind measurements for accurate space weather forecasting, and to observe the continuously full, sunlit disk of Earth from a new and unique vantage point. The DSCOVR mission is a joint venture between NOAA, NASA and the U.S. Air Force. NOAA is operating the spacecraft and performs operational space weather forecasting using the DSCOVR solar wind plasma and interplanetary magnetic field measurements. The Air Force provided the SpaceX Falcon 9 launch vehicle. NASA built the spacecraft, performed on-orbit checkout, and operates the two Earth-facing science instruments –– the Earth Polychromatic Imaging Camera (EPIC) and the NIST Advanced Radiometer (NISTAR). This paper is limited to applications related to the EPIC instrument.

EPIC consists of a 30-cm aperture Cassegrain telescope with a 0.62^O field of view (FOV), which encompasses the Earth having a nominal size of 0.5^O at the L1 vantage point. Light entering the Cassegrain telescope passes through a field-lens group, then a filter wheel, and finally is focused on a hafnium–coated 2048 x 2048 pixel CCD with sensitivity to UV, visible, and near–infrared (NIR) wavelengths. The filter wheel contains 10 narrow band filters from 317.5 nm to 779.5 nm that were designed to obtain products similar to TOMS (Total Ozone Mapping Spectrometer, e.g., Herman et al., 1997) and MODIS (Moderate Resolution Imaging Spectroradiometer, e.g., King et al., 1992). During the refurbishment phase, prior to launch, changes were made that

71   significantly improved EPIC capabilities. The primary changes were a significant

72   reduction of stray light (new filters and field lens group) and addition of the oxygen A-

73   and B-bands to sense cloud and aerosol heights.

74

75   Projected on the three-dimensional (3D) Earth, the sampling size is about 8 km at nadir

76   (near the center of the image), which effectively increases to 10 km when EPIC's point

77   spread function is included. In order to maximize time cadence by reducing transmission

78   time, the images of all wavelength channels, except 443 nm, have been reduced to 1024 x

79   1024 pixels. This yields a resolution of 10 km for the color images, which has been

80   verified by looking at the width of major low latitude rivers in Brazil and Egypt. Of

81   course, the effective resolution is proportional to the secant of the observing angle

82   measured relative to the normal to the Earth's surface (10 km at nadir and 20 km at 60°).

83   The result for 2x2 pixel averaging is a spatial resolution at nadir of about 18 km.

84

85   The Earth-observing geometry of the EPIC instrument is characterized by a nearly

86   constant scattering angle (angle formed between the incident and scattered-to-satellite

87   sunlight vectors) between 168.5° and 175.5°. Figure 1 displays the Sun-Earth View

88   (SEV) angle that is equal to 180° minus scattering angle. The DSCOVR orbit around L1

89   is smaller than that of SOHO (Solar and Heliospheric Observatory) and Wind, but similar

90   to that of ACE (Advanced Composition Explorer). It is important to note that the

91   distance between DSCOVR and Earth changes approximately by 2000-2500 km per day,

92   as part of its non-repeating Lissajous orbit, or about 0.16% of its nominal distance of

93    $1.5x10^6$ km.

94

95   For the 4 UV channels, 317.5, 325, 340, and 388 nm, in-flight radiometric calibration is

96   accomplished by comparison to the reflectance values measured by current well-

97   calibrated Low Earth Orbit (LEO) satellites observing scenes that match in time and

98   observing angles with those from EPIC (Herman et al., 2018, see section 2.3).

99   Calibration of the visible and NIR channels is accomplished using well-calibrated

100 measured earth reflectance values obtained from the Terra and Aqua MODIS LEO

101 satellite observations. Lunar reflectance data are used to help calibrate the two

102 wavelength channels sensitive to the Earth's oxygen absorption (oxygen B- and A-bands:

103 687.75 and 764.0 nm) relative to their adjacent reference channels 680 and 779.5 nm.

104 The details of these calibration procedures are described in Section 2, below.

105

106 There are natural and enhanced color EPIC images provided daily on the

107 https://epic.gsfc.nasa.gov website. The natural color images were created using the bands

108 from EPIC that are within the human visual range. They have been color, contrast and

109 brightness adjusted to represent a human eye would perceive. The RGB ratios of the

110 enhanced color images were processed to emphasize land features. In addition, the

111 Rayleigh molecular scattering and attenuation of solar light by ozone was subtracted.

112 The calculations accounted for Earth's spherical geometry.

113

114 While MODIS on Terra and Aqua cross the equator at 10:30 and 13:30, respectively,

115 DSCOVR/EPIC provides measurements of the sunlit face of Earth from sunrise to sunset.

116 Figure 2 illustrates the key difference between the L1 (EPIC) and LEO (MODIS)

117 observations, where the EPIC's observation of Africa is at 10:56 UTC. Since Terra

118   crosses equator at 10:30, the western part of the left image has a more similar cloud

119   structure with EPIC (middle) than their eastern parts. For Aqua crossing the equator at

120   13:30, the eastern part of the right (MODIS) and middle (EPIC) images are more alike

121   than their western parts.

122

123   The paper structure is the following. Next section discusses EPIC calibration starting

124   from raw data, then the geolocation algorithm for Level 1 data; finally calibration of all

125   EPIC channels converting engineering units of counts/second into reflectance. Section 3

126   describes Level 2 products. First, there are O_3 and Lambert Equivalent Reflectivity

127   retrievals, then SO_2 for volcanic eruptions and aerosol products, including atmospheric

128   correction are discussed. Description of cloud and vegetation Level 2 products completes

129   this section. Section 4 reports on first expected and unexpected capabilities of EPIC

130   observations. Finally, section 5 summarizes the results.

131

132   **2. Calibration**

133   **2.1 Raw EPIC data calibration**

134   Before the raw EPIC data (counts/second) can be used for imagery and quantitative

135   applications, a number of pre-processing steps must be taken. Level-0 EPIC data are

136   converted to Level-1A "corrected count rates" by correcting for detector, electronics, and

137   optics−induced effects. The major steps in the Level-0 to Level-1A conversion are 1)

138   subtracting the dark offset and dark rate signals, 2) correcting electronics signal

139   dependent non-linearity, 3) correcting thermal dependence of the EPIC sensitivity, 4)

140   normalizing by the image integration time, 5) "flat-fielding" in order to remove pixel-to-

141   pixel sensitivity differences, vignetting, and etaloning effects, and 6) correcting stray-

142   light effects to account for light that should be going to a particular pixel, but instead is

143   scattered to other pixels. The dark offset correction utilizes overclock pixels (Habibi,

144   2017) present in each image and the dark rate correction is based on analysis of weekly

145   in-flight shutter-closed dark rate measurements. EPIC non-linearity, temperature

146   sensitivity, and stray light corrections have been derived from pre-launch test data. The

147   EPIC flat-field correction is based on pre-flight test data and updated using analysis of in-

148   flight terrestrial observations taken over the first year of science operations. Finally, for

149   Level-1B data, the radiometric calibration factors for each wavelength channel are

150   determined in terms of EPIC counts/second conversion to reflectance units (Geogdzhayev

151   and Marshak, 2018; Herman et al., 2018).

152

153   **2.2 Geolocation Algorithm for Level-1A/1B Data**

154   EPIC image geolocation is a process which calculates the per-pixel latitude and longitude

155   location for each wavelength's image. This includes both the astronomical calculations

156   to relate the scene to the instrument, as well as heuristical calculations to correct errors

157   beyond the spacecraft instrumentation accuracy and achieve pixel to coordinate accuracy,

158   as well as pixel-to-pixel co-registration between images on different filters. There are a

159   number of challenges to achieving this correction, such as dealing with the rotation of the

160   earth due to the .5-2 minute latency between imaging different wavelengths, correction

161   for spacecraft rotation, jitter, atmospheric refraction correction, as well as an accurate

162   optical model of the telescope. The process of geolocation and georectification requires

163   the images to be accurately mapped to a 3D model of the earth.

164

165

166   The Level 1A algorithm includes all the calculations required for geolocation on the

167   images in their native format. This uses the ephemerides and other spacecraft

168   information to generate a 3D view of the Earth in the same aspect as seen from EPIC at

169   L1. A two-dimensional (2D) transformation of the 3D model, as it would appear on the

170   CCD, is obtained using an instrument optical and model calculation. This 2D

171   transformation in turn provides the per-pixel geodetic coordinates, as well as sun and

172   viewing angles.   Figure 3 depicts this process.

173
174
175   The Level 1B algorithm produces images in which all wavelengths are regridded to the

176   same common grid. This includes correcting the images for changes in the scene due to

177   Earth's rotation, drift in spacecraft pointing, and the spacecraft's own orbital motion. As

178   outlined in Fig. 3, the Level 1B algorithm takes the location information generated and

179   maps the EPIC pixels into 3D models, 1 per band. Each model is then rotated into the

180   same orientation (north up, at a common universal time UT) and then projected and

181   redrawn into a 2D image. The result is all 10 wavelength band images share the same

182   reference grid so that light for each pixel and wavelength comes from the same earth

183   scene. This is essential, since most of the science algorithms rely on ratios of different

184   wavelength channels.

185
186
187   There are still residual issues that affect the geolocation accuracy. This includes errors

188   with the star-tracker pointing, accuracy of the telescope optical model, image time stamps,

189   and effects of atmospheric refraction. Work is currently underway that treats these

190   additional corrections to further improve science products beyond the basic requirements.

191

192   **2.3 Calibration of EPIC UV channels**

193   Since EPIC was launched without an accurate laboratory calibration, in-flight calibration

194   transfer using other well-calibrated satellites was necessary. There were two suitable

195   LEO satellites satellite instruments Aura/OMI (Ozone Monitoring Instrument, e.g. Torres

196   et al., 2007) and Suomi-NPP/OMPS (National Polar-orbiting Partnership / Ozone

197   Mapping and Profiler Suite, e.g., Li et al., 2017) that contain similar wavelength channels

198   and are able to observe scenes that closely match in location and angles with those

199   observed by EPIC. Of these, the best calibrated was OMPS, which has an albedo

200   accuracy of 2% and a wavelength accuracy of better than 1% (Jaross et al., 2014).

201

202   Reflectance calibration was chosen, since the ratio of reflected radiance to the incoming

203   solar flux mostly cancels the strong Fraunhofer line structure. The lack of line structure

204   permits accurate interpolation needed to match the wavelength bands of EPIC. EPIC

205   measures raw counts per second (C/S) based on permanently fixed exposure times

206   designed to fill the CCD wells to approximately 80% for the brightest scenes in each of

207   all 10 channels. Comparison with identical OMPS scenes produces EPIC multiplicative

208   albedo calibration coefficients K_λ (Table 1) to convert C/S into top of the atmosphere

209   reflectance $\pi I_\lambda/S_\lambda$. Here, I_λ is the radiance measured by OMPS at the top of the

210   atmosphere and S_λ is the wavelength dependent solar flux corrected for the sun-earth

211   distance. For the UV channels, there is a small secular change of a few percent per year.

212   A more complete discussion is given in Herman et al. (2018).

213

2.4 Calibration of EPIC visible and near-IR channels

We used MODIS Aqua and Terra L1B 1-km bands 3 (central wavelength is 469 nm), 4

(555 nm), 1 (645 nm) and 2 (858.5 nm) reflectance values to infer calibration factors for

four EPIC visible and near-IR channels: 443, 551, 680 and 780 nm, respectively. For

each EPIC pixel we identified favorable MODIS pixels as follows: (*i*) spatially collocated

within 25 km; (*ii*) temporally collocated within 10 min; and finally, (*iii*) having the same

scattering angles within 0.5^O.

221

We selected EPIC pixels that had at least 40 MODIS pixels within 25 km radius.

Relative standard deviation was then calculated for the matching MODIS and EPIC

pixels. In the latter case, a 5x5 pixel neighborhood was used to calculate the standard

deviation. The value of the relative standard deviation was used to select the most

homogeneous scenes. Two methods were used to determine the calibration coefficients

from the most homogeneous scenes: first, linear regression between EPIC counts and

MODIS reflectance values and second, mean MODIS/EPIC ratio for high MODIS

reflectance (> 0.6) and small relative standard deviation (< 0.1).

230

The differences in the position and spectral width of the corresponding EPIC and MODIS

channels may result in discrepancies when scenes with different spectral signatures are

observed by the two instruments. To compensate, we employ spectral band adjustment

factors (SBAFs) which convert MODIS reflectance values to equivalent EPIC

reflectances for various surface types. These factors, in the form of linear regression

236   coefficients, were obtained from http://www-angler.larc.nasa.gov/SBAF, and are based

237   on the analysis of SCHIAMACHY hyperspectral data (Scarino et al., 2016). To identify

238   the land cover type for each matching EPIC pixel we use a data set developed by

239   Channan et al (2014). The land cover type was identified based on a 0.5x0.5 degree

240   re-projected version of the Global Mosaics of the standard MODIS land cover type data

241   product (MCD12Q1) in the IGBP Land Cover Type Classification. Separate adjustment

242   factors were used for MODIS Aqua and MODIS Terra data (Geogdzhayev and Marshak,

243   2018).

244

245   At the time of this writing, no degradation in the EPIC visible and near-IR bands has

246   been detected, while the UV channels have a very small secular change (Herman et al.,

247   2018). The calibration factors K_λ for these channels are given in Table 2.

248

249   **2.5 Calibration of the EPIC O$_2$ absorbing bands using Lunar observations**

250   To calibrate the EPIC O$_2$ absorbing bands, we used EPIC lunar observations at the time

251   of the Full Moon as seen from the earth. Lunar reflectance R_λ does not increase much

252   with a small wavelength change $\Delta\lambda$; a 10 nm difference in λ leads to a difference in R_λ in

253   the range of 0.0006-0.0013 or 0.8-1.2% (e.g., Ohtake et al., 2010, 2013). It follows from

254   this that the difference in moon reflectance between the O$_2$ B-band (688 nm) and the 'red'

255   (680 nm) channels as well as between the O$_2$ A-band (764 nm) and the near-IR (780 nm)

256   channels will be within 1.5%.

257

258   Since the calibration factors, K_λ, for λ=680 and 780 nm are assumed to be known from

259   in-flight comparisons between EPIC Earth observations and well-calibrated measured

260   Earth reflectances obtained from the Terra and Aqua MODIS LEO satellite observations

261   (see Section 2.4), we can obtain the calibration factors for the O_2 absorbing channels at

262   688 and 764 nm. Indeed, the ratio $F(\lambda_1,\lambda_2)$ of the lunar reflectance values measured in

263   counts/sec at two neighboring channels λ_1 and λ_2 is very stable (Fig. 4). Thus, the

264   calibration factor K_λ for λ=688 nm, can be approximated as

265

266    $$K_{688} = R_{688}/R_{688}^{counts} = R_{688}/[R_{680}^{counts} F(680,688)] =$$

267    $$= [R_{688}/R_{680}] K_{680}/F(680,688) \approx K_{680}/F(680,688).$$

268

269   Similarly to 688 nm, the calibration factor for 764 nm can be estimated as

270

271    $$K_{764} \approx K_{780}/F(780,764).$$

272

273   Here, R_λ and R_λ^{counts} are the values of calibrated reflectance and measured C/S at

274   wavelength λ, respectively; K_λ is the multiplicative calibration coefficient expressed as a

275   conversion from counts/second to reflectance at wavelength λ and the ratio $F(\lambda_1,\lambda_2) =$

276    $R_{\lambda 2}^{counts}/R_{\lambda 1}^{counts}$. The calibration factors K_λ for these channels are given in Table 3.

277

278   The calibration factors for all 10 EPIC channels are also publicly available at

279   https://eosweb.larc.nasa.gov/project/dscovr/DSCOVR_EPIC_Calibration_Factors_V02.p

280   df.

281

282   **3. Products**

3.1 EPIC ozone and Lambert Equivalent Reflectivity retrievals

283

284 Applying the OMPS derived calibration to EPIC's C/S to obtain earth albedos for each of

285 the UV channels, the reflectances can be used to retrieve total column ozone (TCO),

286 Lambert equivalent reflectivity (LER), aerosol optical depth and absorption, aerosol

287 index (AI), and UV reflectance at the Earth's surface (Herman et al., 2018). Ozone

288 retrieval requires the use of measured laboratory high spectral resolution absorption

289 coefficients (Brion et al. (1993, 1998); Daumont et al. (1992); and Malicet et al. (1995)).

290 The EPIC measured reflectance spectra are compared with a set of radiative transfer

291 derived lookup tables for the EPIC filter transmission functions and for a wide range of

292 ozone values. LER, AI, and ozone are retrieved simultaneously with a maximum

293 resolution of 18 km at the sub-satellite point. A matched pair of ozone and LER images

294 are shown in Fig. 5 for August 21, 2016 at 16:58 UT.

295

296 EPIC ozone has been compared to ozone retrieved from a Pandora Spectrometer

297 Instrument (PSI) located in Boulder Colorado (Herman et al., 2015) matched in location

298 and time (UTC) several times per day. The average agreement is 2.1 ± 5.4% (Fig. 6). An

299 additional comparison (Fig. 7) has been made (Herman et al., 2018) with the assimilated

300 ozone product from the Modern-Era Retrospective Analysis for Research and

301 Applications, version 2 (MERRA-2) based on Microwave Limb Sounder (MLS) and total

302 column ozone from the Ozone Monitoring Instrument (OMI). All of the structures in the

303 EPIC ozone retrieval are present in the MERRA-2 assimilation model ozone, but with an

304 average offset of about 3% (10 DU). Comparisons with MERRA-2 have been made

305 using ozone data from other satellites (Wargan et al., 2017) that have similar offsets.

306

3.2 EPIC SO$_2$ retrievals for volcanic eruptions

Volcanic emissions of sulfur dioxide (SO$_2$) and ash have been measured by ultraviolet

(UV) sensors on US and European polar-orbiting satellites since the late 1970s (Bluth et

al., 1993; 1997; Carn et al., 2003; 2015; 2016; Carn and Krotkov, 2016; Guo et al., 2004;

Krotkov et al., 1999a,b; Krueger 1983; 1995; 2000; Li et al., 2017; Pavolonis et al., 2013;

Prata, 1989; Prata and Prata, 2014; Prata and Kerkmann, 2007; Prata et al., 2003; 2015;

Realmuto 2000; Wen and Rose 1994). These observations permit detection of hazardous

volcanic clouds in support of aviation safety management; however, they are generally

available only once a day from LEO satellites with a delay at least 2-3 hours. More

frequent observations can be crucial in providing timely warnings to mitigate threats to

aviation safety. Current geostationary thermal infrared (TIR) imagers including

MSG/SEVIRI, GOES-16/ABI and Himawari-8/AHI can detect and image volcanic SO$_2$

and ash plumes, taking advantage of high frequency observations and low latency to

provide timely warnings to the public, and aviation authorities and operators (Prata 1989;

Realmuto et al., 2000; Ackerman et al., 2008; Pavolonis et al., 2013). DSCOVR/EPIC

provides the first opportunity to observe transient volcanic clouds globally from the L1

Lagrange point. The unique L1 vantage point offers the potential for multiple daily UV

observations of drifting volcanic SO$_2$ and ash clouds globally using a single instrument.

325

The EPIC volcanic SO$_2$ algorithm is a modified version of the heritage Total Ozone

Mapping Spectrometer (TOMS) 4-band algorithm, adapted to the EPIC wavelengths.

The algorithm uses all four EPIC UV channels (317, 325, 340, 388 nm) to retrieve (*i*)

329   vertical column amounts of SO_2 and (*ii*) O_3, (*iii*) the Lambertian equivalent reflectivity

330   (LER) at 388 nm, and (*iv*) its spectral dependence.   The algorithm relies on spectral

331   differences in the SO_2 and O_3 absorption cross sections to simultaneously quantify

332   column amounts of the two gases. SO_2 is more absorbing than O_3 at the shortest UV

333   channel (317 nm), whereas O_3 is more absorbing than SO_2 at the longer channel (325 nm).

334   The retrieval is performed iteratively for each EPIC pixel. It starts with the

335   climatological value of O_3 and zero SO_2 and first computes LER at 388 nm. Because the

336   O_3 and SO_2 absorption are very weak at 388 nm, LER remains fixed during the iterations.

337   The iterations start with climatological values of O_3 and zero SO_2. The algorithm then

338   retrieves adjustments to the initial guess by matching measured and calculated sun-

339   normalized backscattered UV (BUV) radiances in the shorter-wavelength spectral

340   channels (317, 325 and 340 nm). The sensitivities (Jacobians) associated with linear

341   perturbations in SO_2, O_3 and LER are computed for each UV spectral band using pre-

342   computed backscattered UV radiances look-up tables that are numerically interpolated to

343   the EPIC viewing geometry at each iteration. This algorithm appears to have adequate

344   sensitivity to detect moderate to large volcanic eruptions from L1 at solar and view zenith

345   angles less than ~70° (e.g., Fig. 8).

346

347   To increase sensitivity to small eruptions, a simplified version of the SO_2 algorithm has

348   also been developed. It uses the 317 and 388 nm EPIC channels and an a-priori estimate

349   of total ozone. The ozone is re-gridded and smoothed, which reduces channel–to-channel

350   co-location errors. The radiances are normalized accounting for smooth ozone variations,

351 but excluding pixels with elevated SO_2. This error mitigation results in enhanced

352 sensitivity to small volcanic SO_2 clouds.

353

354 No large tropical eruptions have occurred during the DSCOVR/EPIC mission to date (as

355 of January 2018).   However, the sensitivity of EPIC UV radiances to volcanic clouds has

356 been demonstrated by the detection of several mid- to high-latitude eruptions in 2015-

357 2017. Figure 8 shows EPIC SO_2 retrievals for the high-latitude eruption of Pavlof

358 (Alaska, USA) in March 2016. Comparison with the low-Earth orbiting Suomi NPP-

359 OMPS SO_2 data (Fig. 8c) collected at a similar time shows that EPIC clearly detects the

360 proximal volcanic plume where SO_2 columns were highest (>10 Dobson Units: 1DU =

361 2.69×10^{16} molecules SO_2 cm^{-2}), along with some of the distal plume. Note, that the EPIC

362 viewing conditions were not ideal for this eruption, with a relatively high solar zenith

363 angle in Alaska in March, but nevertheless the SO_2 cloud was detected in at least 2 EPIC

364 exposures over approximately a 2-hour period on March 28-29 (Fig. 8 a,b), with the first

365 observation ~90 minutes prior to the SNPP-OMPS overpass. The atmospheric infrared

366 sounder (AIRS) on NASA Aqua satellite also detected the Pavlof SO_2 emissions and a

367 coincident AIRS retrieval on ~23:30 UTC on March 28, using the method of Prata and

368 Bernardo (2007), is shown in Fig. 8d. The total SO_2 mass of 33 kilotons (kT) measured

369 by AIRS compares favorably with the EPIC retrievals, which detected ~25 kT of SO_2.

370

371 These EPIC exposures provide unique observations of SO_2 cloud transport and have great

372 potential to provide new insight into the evolution of volcanic SO_2 emissions, as well as

373 more timely detection and tracking of potentially hazardous volcanic clouds. Forecasting

374   the dispersion of volcanic clouds requires an estimate of the volcanic cloud altitude. The

375   combination of total column SO_2 observations from polar orbiting satellites with

376   trajectory analysis methods has proved useful for estimating volcanic cloud altitudes

377   (Eckhardt et al., 2008; Krotkov et al., 2010; Hughes et al., 2012). Such techniques would

378   be improved by assimilating more frequent observations of volcanic SO_2 from EPIC,

379   enabling more rapid estimation of volcanic cloud altitude.

380
381

382   **3.3 EPIC UV Aerosol Products**

383   A variety of aerosol and aerosol-related products are derived from EPIC's observations.

384   EPIC extends the multi-decadal long UV Aerosol Index (UVAI) record started in 1979

385   with TOMS (Herman et al., 1997; Torres et al., 1998) and currently available from OMI

386   observations (Torres et al., 2007). The EPIC UVAI detects carbonaceous aerosols, desert

387   dust particles, and volcanic ash over the oceans and the continents under both clear and

388   partly cloudy conditions, as well as over extremely bright backgrounds such as snow/ice

389   surfaces and cloud decks. In addition to the qualitative UVAI product, EPIC

390   observations yield aerosol optical depth (AOD) in the UV-VIS range, and near-UV single

391   scattering albedo for both absorbing and non-absorbing aerosol types under cloud-free

392   conditions using a modified version of the OMI aerosol algorithm (Torres et al., 2007;

393   Torres et al., 2013). Because of the sensor's coarse spatial resolution, sub-pixel cloud

394   contamination affects both the frequency of retrievals and the quality of the retrieved

395   aerosol parameters. Figure 9 shows retrievals of UVAI, aerosol optical depth, single

396   scattering albedo and absorption optical depth associated with smoke and desert dust

397   events in Africa.

398

399   Recently developed retrieval approaches are applied to EPIC observations to obtain the

400   optical depth of aerosol layers above clouds, as well as the cloud optical depth unaffected

401   by aerosol absorption effects (Torres et al., 2012; Jethva et al., 2013). Additionally,

402   radiance measurements in the oxygen A- and B-bands are used to simultaneously derive

403   the optical depth and the height of elevated desert dust and smoke aerosol layers over the

404   oceans (Xu, et al., 2017).

405

406   **3.4 Atmospheric Correction Suite**

407   DSCOVR-EPIC is contributing to the Surface Reflectance *Earth System Data Record*.

408   The shortcoming of EPIC's rather coarse spatial resolution is compensated by its high

409   (almost hourly) observation rate, which produces up to 8-12 images of the same area

410   from dawn to dusk, globally. This provides early morning observations, which are

411   unavailable from MODIS or VIIRS, for climatically important tropical regions of the

412   world such as Amazonia where tropical convection generates more clouds in the

413   afternoon. A comparison of statistics between MODIS Terra and Aqua shows about 10%

414   more clouds from MODIS Aqua with equatorial overpass time 13:30 as compared to

415   MODIS Terra crossing equator at 10:30 (Hilker et al., 2015).

416

417   The surface products include spectral bidirectional reflectance factors (BRF, or surface

418   reflectance) and bidirectional reflectance distribution function (BRDF) represented by 3

419   parameters of the Ross-Thick Li-Sparse (Lucht et al., 2000) (RTLS) model. The suite

420 also includes cloud mask and aerosol optical thickness required for atmospheric

421 correction.

422

423 The unique backscattering observation geometry of EPIC will allow us to revisit models

424 of BRDF near the hot-spot direction (scattering angle close to 180 degrees). So far, only

425 a limited analysis has been conducted based on POLDER multi-angle observations (e.g.,

426 Breon et al., 2002). Such models have a high importance for vegetation monitoring in

427 tropics when geometric variation from shifting azimuthal plane overlays seasonal

428 vegetation cycle (e.g., Bi et al., 2016).

429

430 Because EPIC differs significantly from MODIS or VIIRS in spectral bands and spatial

431 and temporal resolution, a new processing algorithm is being developed based on

432 elements of NASA Multi-Angle Implementation of Atmospheric Correction (MAIAC)

433 algorithm originally developed for MODIS (Lyapustin et al., 2011, 2012). The main idea

434 of MAIAC is to take advantage of differences in the space-time variability of atmosphere

435 (aerosols and clouds) and surface to separate their contributions in measured radiance.

436 Such an approach requires observing the same area over time, therefore EPIC processing

437 starts with gridding observations to a 10 km regular sinusoidal grid. Continuous

438 observations of the same grid cell over time yield multi-angle coverage for spectral

439 BRDF retrievals, which then helps cloud detection and aerosol retrievals. MAIAC also

440 characterizes spatial variability between adjacent grid cells under clear skies that helps

441 cloud detection.

442

443   The EPIC MAIAC cloud detection employs a set of tests including absolute brightness

444   test, spatial variability test, oxygen A, B-band test for cirrus detection, and "deviation

445   from expected" test based on our knowledge of spectral surface BRDF which is

446   translated to an expected top-of-atmosphere (TOA) reflectance. An additional filtering

447   takes place during aerosol retrievals and atmospheric correction, which significantly

448   increases overall data quality.

449

450   Aerosol retrieval is based on characterization of the surface spectral reflectance ratios

451   from the time series of EPIC observations using the minimum reflectance method (e.g.,

452   Knapp, 2002). Following aerosol retrievals, the atmospheric correction stage includes

453   BRDF retrieval and computation of surface reflectance (BRF). The BRDF retrieval uses

454   linear inversion to derive three parameters of the RTLS BRDF model from the multi-

455   angle EPIC dataset accumulated from 2-3 days of observations over each 10 km grid cell.

456   A preliminary example of AC processing is shown in Fig. 10. It includes the RGB TOA

457   EPIC image for 27 March 2016 at 1312 UTC (left), the atmospherically corrected land

458   surface RGB image (middle), and retrieved aerosol optical thickness ($AOT_{0.44}$) both over

459   land and ocean on the right.

460

461   **3.5 EPIC Cloud Product**

462   Over the years, cloud products from low Earth orbit (LEO) satellites, such as Terra, Aqua

463   and the NOAA satellites (e.g., Parkinson 2003; Platnick et al. 2003; Heidinger et al.

464   2009) and from geostationary Earth orbit (GEO) satellites, such as GOES (e.g., Schmit et

465   al., 2008, 2017), constitute the main global cloud property database. With the launch of

466   DSCOVR, the EPIC instrument provides new opportunities for cloud related studies,

467   since it covers almost the entire sunlit half of the Earth. Consecutive observations during

468   the day make studying the cloud diurnal cycle on a global scale possible. EPIC cloud

469   products also provide a spatial context for the observations from LEO satellites, because

470   for every LEO observation at daytime, there are always closely collocated EPIC

471   observations. The half-globe synoptic snapshot feature of EPIC makes comparison

472   between synoptic GCM model outputs and observations intuitive (Holdaway and Yang,

473   2016a,b) and helps model validations.

474

475   The EPIC Level 2 cloud products include Cloud Mask (CM), Cloud Effective Pressure

476   (CEP), Cloud Effective Height (CEH), and Cloud Optical Thickness (COT). All the

477   products are provided at the EPIC original temporal and special resolutions. CEP and

478   CEH are derived from the oxygen A- and B-bands, respectively. These data products

479   provide cloud properties of almost the entire sunlit side of the earth, which are important

480   for climate studies, cloud and weather system analysis, and earth radiation budget

481   calculations.

482

483   A suite of algorithms for generating the operational EPIC CM, CEP/CEH and COT

484   products has been developed (Yang et al., 2013; Meyer et al., 2016). (1) The EPIC CM is

485   based on the threshold method; surface is classified into three categories: land, deep

486   water and snow/ice; for each surface type, two independent tests are applied and the final

487   CM with confidence level is determined through combining the results from the two tests.

488   (2) For the CEP/CEH, the Mixed Lambertian-Equivalent Reflectivity (MLER) model

489   (e.g., Koelemeijer et al., 2001; Yang et al., 2013) is adopted, which assumes that an EPIC

490   pixel contains two Lambertian reflectors, the surface and the cloud. This assumption

491   simplifies the radiative transfer equation and cloud pressure can be retrieved using the

492   oxygen A- and B-band pairs. Since the MLER model does not take into account the

493   effect of photon penetration into clouds, the retrieved cloud pressure is an effective

494   pressure. By incorporating the GEOS-5 forecasted atmospheric profiles, the CEP is

495   converted to CEH. (3) The EPIC COT product is produced using the operational MODIS

496   cloud retrieval infrastructure (Platnick et al., 2003). The MODIS system provides

497   simultaneous two-channel retrievals of COT and cloud effective radius (CER), and cloud

498   phase retrievals using a variety of spectral tests. However, since EPIC does not have

499   particle size sensitive channels, a single channel retrieval algorithm was developed

500   assuming fixed values for CER (Meyer et al., 2016). In addition, cloud phase

501   determination capability for EPIC is limited; hence the EPIC COT product provides two

502   retrievals for each cloudy pixel, one assuming liquid phase and the other ice phase. A

503   likely cloud phase is also provided based on the CEH. An example of EPIC cloud

504   products is given in Fig. 11. We note that the relatively big EPIC pixel size (~10 km at

505   nadir) results in large number of partially cloudy pixels. This effect is taken into account

506   in the CEP retrieval as the MLER model derives the effective cloud fraction first (Yang

507   et al., 2013). For COT retrievals, coarser spatial resolution results in a smoother retrieval

508   field compared to the fine resolution MODIS retrievals (Meyer et al., 2016).

509

510   **3.6 EPIC Vegetation Product**

511   The DSCOVR EPIC science product suite includes *Vegetation Earth System Data*

512   *Record* (VESDR) that provides Leaf Area Index (LAI) and diurnal courses of Normalized

513   Difference Vegetation Index (NDVI), Sunlit Leaf Area Index (SLAI) and Fraction of

514   incident Photosynthetically Active Radiation (FPAR) absorbed by the vegetation (Yang

515   et al., 2017). The product at 10 km sinusoidal grid and 65 to 110 minute temporal

516   frequency is generated from the upstream EPIC BRF product (Sect. 3.4). Whereas LAI is

517   a standard product of many satellite missions, global diurnal courses of FPAR, NDVI and

518   SLAI are new satellite derived products (Fig. 12). Sunlit and shaded leaves exhibit

519   different radiative response to incident Photosynthetically Active Radiation (400-700 nm)

520   (Mercado et al., 2009; Stenberg, 1998), which in turn triggers various physiological and

521   physical processes required for the functioning of plants. Leaf area and its sunlit portion

522   are key state parameters in most ecosystem productivity models (Bonan et al., 2003;

523   Chen et al., 2012; Dai et al., 2004; He et al., 2013; Mercado et al., 2009; Norman, 1982)

524   and carbon/nitrogen cycle (Chen et al., 2003; Doughty and Goulden, 2008; Wang et al.,

525   2001).

526

527   Theoretical basis of the operational algorithm is documented in (Yang et al., 2017) and

528   summarized as follows. The Look-up-Table (LUT) approach implemented in the

529   MODIS operational LAI/FPAR algorithm is adopted. The LUT has been significantly

530   modified. First, its parameterization incorporates the canopy hot spot phenomenon (Fig.

531   13) and recent advances in the theory of canopy spectral invariants. This allows more

532   accurate decoupling of the structural and radiometric components of the measured

533   Bidirectional Reflectance Factor (BRF), improves scaling properties of the LUT and

534 consequently simplifies adjustments of the algorithm for data spatial resolution and

535 spectral band compositions. Second, the stochastic radiative transfer equations are used

536 to generate the LUT for all biome types. The equations naturally account for radiative

537 effects of the three-dimensional canopy structure on the BRF and allow for an accurate

538 discrimination between sunlit and shaded leaf areas. Third, the LUT entries are

539 measurable, i.e., they can be independently derived from both below canopy

540 measurements of the transmitted and above canopy measurements of reflected radiation

541 fields. This feature makes possible direct validation of the LUT, facilitates identification

542 of its deficiencies and development of refinements.

543

544 The BRF of the vegetation reaches its maximum in the backscattering directions (Fig. 13).

545 This is the so-called hot spot effect: i.e. a sharp increase in canopy reflected radiation

546 when scattering direction approaches the direction to the sun (Kuusk, 1991; Nilson, 1991;

547 Qin et al., 1996; Ross and Marshak, 1988). The EPIC sensor therefore sees the brightest

548 portion of the canopy reflected radiation. This feature allows us not only to directly

549 obtain sunlit leaf area but also estimate how individual leaves reflect solar radiation,

550 which is unique diagnostic information about leaf biochemical constituents (NRC, 2007,

551 Ustin, 2013). Leaf optical properties can be described by the scattering coefficient,

552 which is the fraction of the canopy intercepted radiation that has been reflected from, or

553 diffusely transmitted through, the canopy (Knyazikhin et al., 2013). Figure 14 shows a

554 false color image (688-551-680) of the scattering coefficient derived from DSCOVR

555 EPIC images (Marshak and Knyazikhin, 2017). The radiation scattered by the vegetation

556 in backscattering directions is very strong, allowing the EPIC to see green leaves even

557 through optically thin-clouds.

558

559 **4. Expected and Unexpected Capabilities**

560 **4.1. Use of the oxygen B-band for monitoring vegetation**

561 The EPIC Normalized Difference Vegetation Index (NDVI), defined (Tucker, 1979) as

562 the ratio between the difference and the sum of the NIR (780 nm) and the red (680 nm)

563 channels, is used to monitor vegetation dynamics. A useful estimate of vegetation

564 density requires an accurate atmospheric correction. However, it was recently shown

565 (Marshak and Knyazikhin, 2017) that if the EPIC O_2 B-band (688 nm) is used instead of

566 the conventional red band 680 nm), the effect of the atmosphere (diffuse radiation) on

567 remote sensing of surface reflectance is reduced and the residual uncertainties in

568 atmospheric correction can be better tolerated. This is due to two factors: (*i*) the

569 vegetated surface is sufficiently dark at 688 nm, and (*ii*) the O_2 absorbing atmosphere

570 substantially reduces multiple scattering. Note that also at the slightly longer wavelength

571 of 688 nm, there is less Rayleigh and aerosol scattering.

572

573 To support this statement, the spectral invariant approximation to the bidirectional

574 reflection factor (BRF) of vegetated surface (Knyazikhin et al., 2011; Stenberg et al.,

575 2016; Yang et al., 2017) was used. It was shown that the retrieval of a spectrally

576 invariant coefficient (Marshak and Knyazikhin, 2017) determined by purely canopy

577 structure is only weakly sensitive to the uncertainties in the spectral properties of the

578 atmospheric optical depth above the canopy. On the other hand, the spectral scattering

579   coefficients at the EPIC green to NIR spectral bands are fully determined by the

580   chlorophyll absorption spectrum and can be estimated from the TOA BRF and the

581   approximated spectrally invariant coefficient (Fig. 14). It was demonstrated (Marshak

582   and Knyazikhin, 2017) that the approximated values of spectral scattering coefficient

583   at 551, 688 and 780 nm fit well the spectral shape of the 'true' scattering coefficient over

584   vegetated land for all atmospheric conditions observed. The spectral signature of the

585   chlorophyll absorption at these wavelengths is unique to green leaves. Consequently, the

586   spectral scattering coefficient of the vegetated surface differs significantly from any one

587   of other types of reflecting media, as illustrated in Fig. 14.

588

589   Figure 15 illustrates with two NDVIs with 780&680 (middle panel) and 780&688 (right

590   panel) over Africa that the 780&688 NDVI better identifies patterns of dense vegetation

591   compared to the 780&680 NDVI. This is because without an accurate atmospheric

592   correction the 780&688 NDVI is more sensitive to the presence of the chlorophyll than

593   the standard 780&680 one.

594

595   **4.2 Detection of oriented ice crystals from 1.5 million km away**

596   Many DSCOVR/EPIC images contain unexpected bright flashes of light over land, not

597   usually seen by other satellites. Figure 16 provides an example of such flashes. Here we

598   focus on flashes only over land so as not to be confused with glints over ocean water.

599   Marshak et al. (2017) constructed a yearlong time series of flash latitudes, scattering

600   angles and oxygen absorption to demonstrate conclusively that the flashes over land are

601   specular reflections off tiny ice platelets, floating in air nearly horizontally.

602

603   The time series of latitudes of the detected flashes corresponds to a set of latitudes that

604   permit specular reflection for a given time of year. As the Earth's axial tilt (23.4°) causes

605   local zenith directions to vary, the glints reach their southernmost of ~25° S around

606   December 22 and their northernmost latitude of ~25° N around June 22. The detected

607   glints are near the equator around the equinoxes in March and September. The almost

608   complete coincidence of the measured latitudes with the theoretical curve constituted

609   compelling evidence for the ice crystal specular reflection hypothesis.

610

611   In addition, using EPIC measurements of absorption by molecular oxygen (O_2) via the

612   ratio of absorbing channel to adjacent non-absorbing channel reflectances, cloud height

613   was estimated for all detected flashes. Compared with radiative transfer simulations of

614   EPIC O_2 A- and B-band ratios, it was shown that that the glints occur within medium-

615   high clouds that are most likely to contain horizontally oriented ice platelets.

616

617   While we are not aware of any deep space or geostationary observations (36000 km)

618   observations of glint off tropospheric ice clouds reported in the literature, atmospheric

619   observations of such specular ice reflections have been made with ground-based lidars

620   (Sassen and Benson, 2001) and by satellites on low-Earth orbit: POLDER (Polarization

621   and Directionality of the Earth's Reflectances) polarized measurements (Chepfer et al.,

622   1999; Breon and Dubrulle, 2004; Noel and Chepfer, 2004), and CALIPSO (Cloud-

623   Aerosol Lidar and Infrared Pathfinder Satellite Observation) lidar returns (Noel and

624 Chepfer, 2010). All such cloud glint observations are bounded by an altitude of about

625 700 km and have broader angular resolution than EPIC.

626

627 Based on in-situ measurements of cirrus clouds (e.g., Korolev et al., 2000), tiny

628 hexagonal platelets of ice, floating in air in nearly perfect horizontal alignment are likely

629 responsible for the glints observed by EPIC over land. Cirrus clouds permanently cover

630 more than 30% of the Earth surface and play a major role in the Earth's radiation budget

631 (Stephens et al., 1990). Most of these clouds are composed of nonspherical ice crystals.

632 The orientation of these crystals is difficult to detect; however, oriented particles create a

633 very strong specular reflection (Yang et al., 2003) and, if their concentration is large

634 enough, it can substantially increase cloud albedo compared to randomly oriented crystals.

635

636 **4.3 EPIC Erythemal Irradiance**

637 Synoptic ozone and cloud reflectivity and cloud transmission have been determined for

638 most days during the current operating lifetime of DSCOVR. These may be used to

639 estimate the erythemal irradiance at the earth's surface as a function of latitude, longitude

640 (time of day), and altitude (Herman et al., 2018). The method is based on previous

641 calculations (Herman, 2010) applied to polar orbiting satellites that measured ozone and

642 reflectivity at 13:30 local time and then assumed that the same values applied to noon.

643 The noon assumption can be applied to slowly varying ozone, but is not accurate for

644 estimating the effects of cloud transmission T from rapidly varying cloud cover. This is

645 especially true for local times other than noon. The calculation method outlined here for

646 erythemal irradiance can be easily extended to other processes dependent on a

647   wavelength dependent action spectrum (Herman, 2010). Using the spectrally weighted

648   erythemal Action spectrum $A_{ERY}(\lambda)$, the erythemal irradiance is derived from an integral

649   over UV wavelengths λ,

$$E_0(\theta,\Omega,T) = \int_{250}^{400} I(\lambda,\theta,\Omega,T)A(\lambda)d\lambda$$

$250 < \lambda < 298$ nm $\log_{10}(A_{ERY}) = 0$

$298 < \lambda < 328$ nm $\log_{10}(A_{ERY}) = 0.094\ (298 - \lambda)$

$328 < \lambda < 400$ nm $\log_{10}(A_{ERY}) = 0.015\ (139 - \lambda)$

650    $E_0(\theta,\Omega,T)$ is the erythemal irradiance at sea level from a radiative transfer calculation

651   (Herman, 2010). The erythemal weighting function $\log_{10}(A_{ERY}(\lambda))$ is given by the

652   standard fitting function (McKinley and Diffey, 1987). At altitude z, the calculation of

653   erythemal irradiance $E(\theta,\Omega,z,T)$ (W/m^2) is defined in terms of the product $E_0(\theta,\Omega,T)$ x

654    $H(\theta,\Omega,z)$, where $H(\theta,\Omega,z) = 1 + f(\theta,\Omega,z)$. Here f is the fractional increase of E_0 as a

655   function of altitude for specified solar zenith angle θ and ozone amount Ω. The details

656   and computational method are described in Herman (2010) and with extensions for

657    $H(\theta,\Omega,z)$ in Herman et al. (2018).

658

659   An example of $E(\theta,\Omega,z,T)$ is shown in Fig. 17a for April 1, 2016 at 17:16 UTC. Local

660   noon is near the center of the image with sunrise to the left (west) and sunset to the right

661   (east). For this date, the sun is overhead just north of the equator producing very high

662   values of erythemal irradiance $E(\theta,\Omega,z,T)$ corresponding to a UV index, UVI, of 13 at sea

663   level in the Pacific Ocean (UVI = 40 $E(\theta,\Omega,z,T)$). Higher values (UVI=16) are seen in

664   the Sierra Nevada Mountains in Mexico near 20°N. This particular day has some small

665 clouds over most of South America except for thick clouds over eastern Argentina. For

666 the erythemal irradiance, the presence of clouds reduces the amount of UV reaching the

667 ground (blue color with a UV index of less than 4).

668

669 The increase with altitude is much more pronounced during the summer months over the

670 Andes Mountains reaching above 4 km (over 13,000 feet). Figure 17b shows the large

671 increases with altitude over the Andes Mountains for November 27, 2016, with the sun

672 nearly overhead at 20^oS latitude. Here the UV index ranges from 16 to 18, which agrees

673 with previous ground-based measurements in this region (Cede et al., 2002). In the

674 completely clear regions of the Andes Mountains the UV index is even higher than 18.

675

676 **5. Summary**

677 DSCOVR was launched on February 11, 2015 into a L1 orbit, about 1.5 million

678 kilometers from Earth towards the Sun to provide continuous solar wind measurements

679 and to observe the sunlit disk of Earth from a new and unique vantage point. The

680 observation of the rotating sunlit face of the Earth is done by the DSCOVR/EPIC

681 instrument, a 10-filter spectroradiometer (317.5 to 780 nm) with a maximum resolution

682 of 10x10 km^2 for 443 nm at the sub-satellite point; the other 9 reduced resolution

683 channels have 18x18 km^2 resolution. The main difference with Low Earth Orbit satellites

684 (LEO) is that EPIC observes the full sunlit face of the Earth from sunrise to sunset at near

685 backscattering directions (the scattering angle is between 168.5^o and 175.5^o). The

686 frequency of EPIC observations is 68 to 110 minutes depending on the season (more

687 frequently in summer, from mid-April to mid-October).

688

689   The EPIC in-flight calibration is done by comparison with well-calibrated LEO satellites:

690   Aura/OMI, Suomi-NPP/OMPS for UV bands, Terra/MODIS and Aqua/MODIS for

691   visible and near-IR bands. The calibration of O_2 absorbing bands are generated using the

692   calibrated neighboring channels and EPIC Lunar observations assuming that a 10 nm

693   difference in wavelength leads to a difference in reflectance of only 1%.

694

695   Calibrated EPIC measurements are used to produce several EPIC products including

696   ozone, erythemal irradiance, SO_2, aerosol, cloud and vegetation properties.   In particular,

697   total ozone level and SO_2 retrievals for volcanic eruptions, UV aerosol index, UV total

698   and absorption optical depths, UV single scattering albedo, surface spectral reflectance

699   and aerosol optical depth in visible channels, cloud mask, cloud optical depth and cloud

700   height, and, finally, vegetation and sunlit leaf area index and fraction of incident

701   photosynthetically active radiation absorbed by vegetation. Some of these products are

702   unique, e.g., the sunlit portion of the leaf area. As a matter of fact, sunlit and shaded

703   leaves exhibit different radiative response to incident radiation and sunlit fraction of leaf

704   area index is the key parameter in ecosystem productivity model. Other parameters are

705   also retrieved from LEO measurements, but a unique DSCOVR observational strategy

706   (backscattering direction and sunrise to sunset observations) leads an innovative

707   characterization of many of retrieved parameters.

708

709   There are well-expected and completely unexpected discoveries made from EPIC

710   observations. For example, since oxygen absorption in the B-band reduces the

contribution of multiple scattering (and diffuse radiation), we were able to use O_2 B-band

(688 nm) to monitor vegetation instead of a red (680 nm) channel without requiring an

atmospheric correction. We were able to explain the bright flashes of light over land seen

in EPIC RGB imagery as specular reflection of tiny ice crystals floating nearly

horizontally (Marshak et al., 2017). Finally, because of EPIC's L1 orbit, we were able to

estimate the erythemal irradiance and the daily variation of UV radiances from sunrise to

sunset to measure skin reddening and potential sunburn from sunlight.

References

Ackerman, S. A., Schreiner, A.J., Schmit, T. J., Woolf, H. M., Li, J., and Pavolonis, M.,

    2008: Using the GOES sounder to monitor upper level SO2 from volcanic

    eruptions. *J. Geophys. Res. Atmos.*, 113, doi:10.1029/2007JD009622.

Bi, J., R. Myneni, A. Lyapustin, Y. Wang, T. Park, C. Chen, K. Yan, Y. Knyazikhin,

    2016: Amazon forests' response to droughts: a perspective from the MAIAC

    product, *Remote Sens.,* 8, 356; doi:10.3390/rs8040356.

732   Bluth, G.J.S., C.C. Schnetzler, A.J. Krueger, and L.S. Walter, 1993: The contribution of

733   explosive volcanism to global atmospheric sulphur dioxide concentrations, *Nature*,

734   366, 327-329.

735   Bluth, G.J.S., W.I. Rose, I.E. Sprod, and A.J. Krueger, 1997: Stratospheric loading of

736   sulfur from explosive volcanic eruptions, *Journal of Geology*, 05, 671-683.

737   Bonan, G.B., Levis, S., Sitch, S., Vertenstein, M., & Oleson, K.W., 2003: A dynamic

738   global vegetation model for use with climate models: concepts and description of

739   simulated vegetation dynamics. *Global Change Biology, 9*, 1543-1566.

740   Bréon, F.-M., F. Maignan, M. Leroy, and I. Grant, 2002: Analysis of hot spot directional

741   signatures   measured   from   space,   *J.   Geophys.   Res.,*   107(D16),

742   doi:10.1029/2001JD001094.

743   Breon, F.-M., and B. Dubrulle, 2004: Horizontally oriented plates in clouds, *J. Atm. Sci.*,

744   61, 2888–2898.

745   Brion, J., Chakir, A., Daumont, D., Malicet, J., and Parisse, C., 1993: High-resolution

746   laboratory absorption cross section of O3. Temperature effect, *Chem. Phys. Lett.*,

747   213, 610–612.

748   Brion, J., Chakir, A., Charbonnier, J., Daumont, D., Parisse, C., and Malicet, J., 1998:

749   Absorption spectra measurements for the ozone molecule in the 350–830 nm

750   region, *J. Atmos. Chem.*, 30, 291–299.

751   Broadbent, Arthur D. A critical review of the development of the CIE1931 RGB color-

752   matching functions, 2004: *Color Research & Applications*, 29 (4): 267–272.

753   doi:10.1002/col.20020.

754   Carn, S. A., A. J. Krueger, G. S. J. Bluth, S. J. Schaefer, N. A.Krotkov, I. M. Watson, and

755   S. Datta (2003), Volcanic eruption detection by the Total Ozone Mapping

756   Spectrometer (TOMS) instruments: A 22-year record of sulfur dioxide and ash

757   emissions, in Volcanic Degassing, Special Publication of the Geological Society

758   of London No. 213, 2003: edited by C. Oppenheimer, D. M. Pyle, and J. Barclay,

759   177-202, Geological Society, London, UK, 10.1144/GSL.SP.2003.213.01.11.

760   Carn, S.A. and N.A. Krotkov, 2016: UV Satellite Measurements of Volcanic Ash, In: S.

761   Mackie, K. Cashman, A. Rust, H. Ricketts and I.M. Watson (eds.), Volcanic ash:

762   Hazard Observation, Elsevier, pp. 217-231, doi:10.1016/B978-0-08-100405-

763   0.00018-5.

764   Carn, S.A., Clarisse, L., & Prata, A. J., 2016: Multi-decadal satellite measurements of

765   global volcanic degassing. *Journal of Volcanology and Geothermal Research*,

766   311, 99–134, 2016.

767   Cede, A., E. Luccini, R. D. Piacentini, L. Nuñez, and M. Blumthaler, 2002: Monitoring

768   of Erythemal Irradiance in the Argentine Ul- traviolet Network, *J. Geophys. Res.,*

769   107, AAC 1-1–AAC 1-10, https://doi.org/10.1029/2001JD001206.

770   Chen, J.M., Liu, J., Leblanc, S.G., Lacaze, R., & Roujean, J.-L., 2003: Multi-angular

771   optical remote sensing for assessing vegetation structure and carbon absorption.

772   *Remote Sensing of Environment, 84*, 516-525.

773   Chen, J.M., Mo, G., Pisek, J., Liu, J., Deng, F., Ishizawa, M., & Chan, D., 2012: Effects

774   of foliage clumping on the estimation of global terrestrial gross primary Eckhardt,

775   S., A. J. Prata, P. Seibert, K. Stebel, and A. Stohl (2008), Estimation of the

776   vertical profile of sulfur dioxide injection into the atmosphere by a volcanic

777   eruption using satellite column measurements and inverse transport modeling,

778   *Atmos. Chem. Phys.,* 8(14), 3881–3897.

779   Chepfer, H., G. Brogniez, P. Goloub, F. M. Breon, and P. H. Flamant, 1999:

780   Observations of horizontally oriented ice crystals in cirrus clouds with POLDER-

781   1/ADEOS-1. *J. Quant. Spectrosc. Radiat. Transfer*, **63**, 521–543.

782   Dai, Y., Dickinson, R.E., & Wang, Y.-P., 2004: A two-big-leaf model for canopy

783   temperature, photosynthesis, and stomatal conductance. *J. Climate, 17*, 2281-2299.

784   Daumont, D., Brion, J., Charbonnier, J., and Malicet, J., 1992: Ozone UV spectroscopy I:

785   Absorption cross-sections at room temperature, *J. Atmos. Chem*., 15,145–1552.

786   Doughty, C.E. and Goulden, M.L., 2008: Seasonal patterns of tropical forest leaf area

787   index and CO2 exchange. *J. Geophys. Res.: Biogeosciences* (2005–2012), 113.

788   Geogdzhayev, I. and A. Marshak, 2018. Calibration of the DSCOVR EPIC visible and

789   NIR channels using MODIS Terra and Aqua data and EPIC lunar observations.

790   *Atmos. Meas. Tech.* 11, 359-368, https://doi.org/10.5194/amt-11-359-2018.

791   Guo, S., Bluth, G. J. S., Rose, W. I., Watson, I. M., and Prata, A. J., 2004: Re-evaluation

792   of SO2 release of the 15 June 1991 Pinatubo eruption using ultraviolet and

793   infrared satellite sensors, *Geochem. Geophys. Geosys*. 5(4), Q04001,

794   doi:10.1029/2003GC000654.

795   Habibi, Mehdi, 2017: Image Sensors *in Measurement, Instrumentation, and Sensors*

796   Handbook, Second Edition, John G. Webster, Halit Eren, Ed., CRC Press, 46-4.

797   He, M., Ju, W., Zhou, Y., Chen, J., He, H., Wang, S., Wang, H., Guan, D., Yan, J., & Li,

798   Y., 2013: Development of a two-leaf light use efficiency model for improving the

799   calculation of terrestrial gross primary productivity. *Agricultural and forest*

800   *meteorology*, 173, 28-39.

801   Heidinger, A. K., & Pavolonis, M. J., 2009: Gazing at cirrus clouds for 25 years

802   through a split window. Part I: Methodology. *J. Applied Meteorology and*

803   *Climatology,* 48, 1100–1116.

804   Herman, J.R., P.K. Bhartia, O. Torres, C. Hsu , C. Seftor, and E. Celarier, Global

805   Distribution of UV-absorbing Aerosols From Nimbus-7/TOMS data, 1997: *J.*

806   *Geophys. Res*., 102, 16911-16922.

807   Herman, J.R., 2010: Use of an improved radiation amplification factor to estimate the

808   effect of total ozone changes on action spectrum weighted irradiances and an

809   instrument response function, *J. Geophys. Res.,* D23119,

810   doi:10.1029/2010JD014317.

811   Herman, J.R., R.D. Evans, A. Cede, N.K. Abuhassan, I. Petropavlovskikh, and G.

812   McConville, 2015: Comparison of Ozone Retrievals from the Pandora

813   Spectrometer System and Dobson Spectrophotometer in Boulder Colorado, *Atmos.*

814   *Meas. Tech.*, 8, 3407–3418, 2015 doi:10.5194/amt-8-3407-2015

815   Herman, J.R., L. Huang, R.D. McPeters, J. Ziemke, A. Cede, and K. Blank, 2018:

816   Synoptic ozone, cloud reflectivity, and erythemal irradiance from sunrise to

817   sunset for the whole Earth as viewed by DSCOVR spacecraft from the earth-sun

818   Lagrange-1, *Atmos. Meas. Tech.,* 11, 1-

819   18, https://avdc.gsfc.nasa.gov/pub/DSCOVR/JayHerman/.

820   Hilker, T., A. I. Lyapustin, Y. Wang, F. G. Hall, C. J. Tucker, P. J. Sellers, 2015: On the

821   measurability of change in Amazon vegetation from MODIS, *Remote Sens.*

822   *Environ.*, 166, 233-242.

823   Holdaway, D. and Y. Yang, 2016a: Study of the Effect of Temporal Sampling Frequency

824   on DSCOVR Observations Using the GEOS-5 Nature Run Results (Part II):

825   Cloud Coverage. *Remote Sens., 8*(5), 431, doi:10.3390/rs8050431.

826   Holdaway, D. and Y. Yang, 2016b: Study of the Effect of Temporal Sampling Frequency

827   on DSCOVR Observations Using the GEOS-5 Nature Run Results (Part I):

828   Hughes, E. J., L. C. Sparling, S. A. Carn, and A. J. Krueger, 2012: Using horizontal

829   transport characteristics to infer an emission height time series of volcanic SO2, *J.*

830   *Geophys. Res.,* 117, D18307, doi:10.1029/2012JD017957.

831   Jaross, G., P. K. Bhartia, G. Chen, M. Kowitt, M. Haken, Z. Chen, P. Xu, J. Warner,

832   and T. Kelly, 2014: OMPS Limb Profiler instrument performance assessment, *J.*

833   *Geophys. Res. Atmos.*, 119, 4399–4412, doi:10.1002/2013JD020482.

834   Jethva, H., O. Torres, L. Remer, and P.K. Bhartia, 2013: A color ratio method for

835   simultaneous retrieval of aerosol and cloud optical thickness of above-cloud

836   absorbing aerosols from passive sensors: Application to MODIS measurements,

837   *IEEE Transactions on Geoscience and Remote Sensing*, Vol 51, 7, 3862-3870.

838   King, M. D, Y. J. Kaufman, W. P. Menzel, D. Tandre, 1992: Remote – sensing of cloud,

839   aerosol, and water –vapor properties from the Moderate Resolution Imaging

840   Spectroradiometer (MODIS). *IEEE Trans. Geoscience. Remote Sens.*, 30, 2-27.

841   Knapp, K. R., 2002: Quantification of aerosol signal in GOES 8 visible imagery over the

842   United States, *J. Geophys. Res*., 107(D20), 4426, doi:10.1029/2001JD002001.

843   Knyazikhin, Y., Schull, M.A., Stenberg, P., Mõttus, M., Rautiainen, M., Yang, Y.,

844   Marshak, A., Latorre Carmona, P., Kaufmann, R.K., Lewis, P., Disney, M.I.,

845   Vanderbilt, V., Davis, A.B., Baret, F., Jacquemoud, S., Lyapustin, A., & Myneni,

846   R.B., 2013: Hyperspectral remote sensing of foliar nitrogen content. *Proceedings*

847   *of the National Academy of Sciences, 110*, E185-E192.

848   Knyazikhin, Y., Schull, M.A., Xu, L., Myneni, R.B., & Samanta, A., 2011: Canopy

849   spectral invariants. Part 1: A new concept in remote sensing of vegetation.

850   *Journal of Quantitative Spectroscopy and Radiative Transfer, 112*, 727-735.

851   Koelemeijer, R. B. A., P. Stammes, J. W. Hovenier, and J. F. de Haan, 2001: A fast

852   method for retrieval of cloud parameters using oxygen A band measurements

853   from the Global Ozone Monitoring Experiment, *J. Geophys. Res.,* 106, 3475–

854   3490.

855   Korolev, A., G. A. Isaac, and J. Hallett, 2000: Ice particle habits in stratiform clouds.

856   *Quart. J. Roy. Meteor. Soc*., **126**, 2873–2902.

857   Krotkov, N. A., O. Torres, C. Seftor, A. J. Krueger, A. Kostinski, W. I. Rose, G. J. S.

858   Bluth, D. Schneider, and S. J. Schaefer, 1999a: Comparison of TOMS and

859   AVHRR volcanic ash retrievals from the August 1992 eruption of Mt. Spurr,

860   *Geophys. Res. Lett.*, 26(4), 455–458.

861   Krotkov, N.A., D.E. Flittner, A.J. Krueger, A. Kostinski, C. Riley and W. Rose, O.

862   Torres, 1999b: Effect of particle non-sphericity on satellite monitoring of drifting

863   volcanic ash clouds, *JQSRT*, 63, 613-630.

864   Krotkov, N. A., M. R. Schoeberl, G. A. Morris, S. Carn, and K. Yang, 2010: Dispersion

865   and lifetime of the SO2 cloud from the August 2008 Kasatochi eruption, *J.*

866   *Geophys. Res.,* 115, D00L20, doi:10.1029/2010JD013984.

867   Krueger, A.J., 1983: Sighting of El Chichón sulfur dioxide clouds with the Nimbus 7

868   Total Ozone Mapping Spectrometer, *Science*, 220, p. 1377-1378.

869   Krueger, A. J., Walter, L. S., Bhartia, P. K., Schnetzler, C. C., Krotkov, N. A., Sprod, I.,

870   and Bluth, G. J. S.,1995: Volcanic sulfur dioxide measurements from the total

871   ozone mapping spectrometer instruments, *J. Geophys. Res.,* 100(D7), 14,057-

872   14,076.

873   Krueger, A. J., S. J. Schaefer, N. Krotkov, G. Bluth, and S. Baker, 2000: Ultraviolet

874   remote sensing of volcanic emissions, in Remote Sensing of Active Volcanism,

875   Geophys. Monogr. Ser., 116, Ed. P. J. Mouginis-Marks, J. A. Crisp and J. H. Fink,

876   25–43, AGU, Washington, D. C., 2000.

877   Kuusk, A., 1991: The Hot Spot Effect in Plant Canopoy reflectance. In R.B. Myneni, & J.

878   Ross (Eds.), *Photon-vegetation interactions: applications in plant physiology and*

879   *optical remote sensing* (pp. 139-159). Berlin Heidelberg: Springer-Verlag

880   Li, C., Krotkov, N. A., Carn, S., Zhang, Y., Spurr, R. J. D., and Joiner, J.: New-

881   generation NASA Aura Ozone Monitoring Instrument (OMI) volcanic SO_2

882   dataset: Algorithm description, initial results, and continuation with the Suomi-

883   NPP Ozone Mapping and Profiler Suite (OMPS), 2017: *Atmos. Meas. Tech*., 10,

884   445-458, doi:10.5194/amt-10-445-2017.

885   Lucht, W., Schaaf C. B., Strahler A. H., 2000: An algorithm for the retrieval of albedo

886   from space using semiempirical BRDF models. *IEEE Trans. Geosci. Remote*

887   *Sens.*, 38, 977-998.

888   Lyapustin, A., Y. Wang, I. Laszlo, R. Kahn, S. Korkin, L. Remer, R. Levy, and J. S. Reid,

889   2011: Multi-Angle Implementation of Atmospheric Correction (MAIAC): Part 2.

890   Aerosol Algorithm, *J. Geophys. Res.*, 116, D03211, doi:10.1029/2010JD014986.

891   Lyapustin, A., Y. Wang, I. Laszlo, T. Hilker, F. Hall, P. Sellers, J. Tucker, S. Korkin,

892   2012: Multi-Angle Implementation of Atmospheric Correction for MODIS

893   (MAIAC). 3: Atmospheric Correction. *Rem. Sens. Environ.*,

894   http://dx.doi.org/10.1016/j.rse.2012.09.002.

895   Malicet, J., Daumont, D., Charbonnier, J., Chakir, C., Parisse, A.,and Brion, J.: Ozone

896   UV Spectroscopy.II: Absorption cross sectionsand temperature dependence,

897   1995: *J. Atmos. Chem.*, 21, 263–273.

898   Marshak, A. and Knyazikhin, Y., 2017: The spectral invariant approximation within

899   canopy radiative transfer to support the use of the EPIC/DSCOVR oxygen B-band

900   for monitoring vegetation. *J. Quant. Spectrosc. Radiat. Transfer, 191*, 7-12

901   Marshak, A., T. Varnai and A. Kostinski, 2017: Terrestrial glint seen from deep space:

902   oriented ice crystals detected from the Lagrangian point. *Geoph. Res. Lett.*, 44,

903   doi:10.1002/2017GL073248.

904   McKinley, A. F. and B. L. Diffey, 1987: A reference action spectrum for ultraviolet

905   induced erythema in human skin, in: Human Exposure to Ultraviolet Radiation:

906   Risks and Regulations, edited by: Passchier, W. R. and Bosnjakovic, B. F. M.,

907   Elsevier, Amsterdam, 83–87.

908   Mercado, L.M., Bellouin, N., Sitch, S., Boucher, O., Huntingford, C., Wild, M., & Cox,

909   P.M.. 2009: Impact of changes in diffuse radiation on the global land carbon sink.

910   *Nature, 458*, 1014-1017.

911   Meyer, K., Y. Yang, and S. Platnick, 2016: Uncertainties in cloud phase and optical

912   thickness retrievals from the Earth Polychromatic Imaging Camera (EPIC), *Atmos.*

913   *Meas. Tech.,* 9, 1785-1797, doi:10.5194/amt-9-1785-2016.

914   Nilson, T., 1991: Approximate Analytical Methods for Calculating the Reflection

915   Functions of Leaf Canopies in Remote Sensing. In R.B. Myneni, & J. Ross (Eds.),

916   *Photon-vegetation interactions: applications in plant physiology and optical*

917   *remote sensing* (pp. 161-190). Berlin Heidelberg: Springer-Verlag.

918   Noel, V., and H. Chepfer, 2004: Study of ice crystal orientation in cirrus clouds based on

919   satellite polarized radiance measurements. *J. Atmos. Sci.,* **61**, 2073-2081.

920   Noel, V., and H. Chepfer, 2010: A global view of horizontally oriented crystals in ice

921   clouds from Cloud-Aerosol Lidar and Infrared Pathfinder Satellite Observation

922   Norman, J.M., 1982: Simulation of microclimates. *Biometeorology in integrated pest*

923   *management*, 65-99.

924   NRC (2007). *Earth Science and Applications from Space: National Imperatives for the*

925   *Next Decade and Beyond.* Washington, DC: The National Academies Press.

926   https://doi.org/10.17226/11820.

927   Ohtake, M., T. Matsunaga, Y. Yokota, S. Yamamoto, Y. Ogawa, T. Morota, C. Honda, J.

928   Haruyama, K. Kitazato, H. Takeda, A. Iwasaki, R. Nakamura, T. Hiroi, S.

929   Kodama and H. Otake, 2010. Deriving the absolute reflectance of lunar surface

930   using SELENE (Kaguya) Multiband Imager data. *Space Sci. Rev.* 154, 57-77.

931   Ohtake M., C.M. Pieters, P. Isaacson, S. Besse, Y. Yokota, T. Matsunaga, J. Boardman,

932   S. Yamomoto, J. Haruyama, M. Staid, U. Mall and R.O. Green, 2013, One Moon,

933   many measurements 3: Spectral reflectance. *Icarus*, 226, 364-374.

934   Pavolonis, M., A. Heidinger, and J. Sieglaff, 2013: Automated retrievals of volcanic ash

935   and dust cloud properties from upwelling infrared measurements, *J. Geophys. Res.*

936   *Atmos.*, 118, 1436–1458, doi:10.1002/jgrd.50173.

937   Parkinson, C. L., 2003: Aqua: An Earth-observing satellite mission to examine water and

938   other climate variables*, IEEE Trans. Geosci. Remote Sens., 41,* 173–*183,* doi:

939   10.1109/TGRS.2002.80831

940   Platnick, S., M. D. King, S. A. Ackerman, W. P. Menzel, B. A. Baum, J. C. Riédi, and R.

941   A. Frey, 2003: The MODIS cloud products: Algorithms and examples from Terra,

942   *IEEE Trans. Geosci. Remote Sens.*, *41*, 459-473, doi:10.1109/TGRS.2002.808301.

943   Prata, A. J., 1989: Observations of volcanic ash clouds in the 10-12μm window using

944   AVHRR/2 data, *Int. J. Rem. Sens.*, 10, 751-776.

945   Prata, A. J., Rose, W. I., Self, S., and D. M. O'Brien, 2003: Global, long-term sulphur

946   dioxide measurements from TOVS data: A new tool for studying explosive

947   volcanism and climate, In Volcanism and the Earth's Atmosphere (ed. Robock

948   and Oppenheimer), Geophysical Monograph. 139, 75-92.

949   Prata, A. J., and Bernardo, C.: Retrieval of volcanic SO_2 column abundance from

950   Atmospheric Infrared Sounder data, *J. Geophys. Res.*, 112, D20204,

951   doi:10.1029/2006JD007955, 2007.

952   Prata, A.J. and Kerkmann, J., 2007: Simultaneous retrieval of volcanic ash and SO2 using

953   MSG-SEVIRI measurements. *Geoph. Res. Lett.*, 34, L05813,

954   http://doi.org/10.1029/2006GL028691.

955   Prata, A. J and Prata, G. S., 2014:Remote sensing of volcanic ash and sulphur dioxide, In

956   "Volcanism and Global Environmental Change" (*Ed. Scmidt, A.and Fristad, K.*).

957   Prata, A., Bluth, G. J. G., Werner, C., Realmuto, V., Carn, S & Watson, M., 2015:

958   Remote sensing of gas emissions from volcanoes. In Monitoring Volcanoes in the

959   North Pacific (pp. 145-186). Springer Berlin Heidelberg.

960   Qin, W., Goel, N.S., & Wang, B., 1996: The hotspot effect in heterogeneous vegetation

961   canopies and performances of various hotspot models. *Remote Sen. Reviews, 14*,

962   283-332.

963   Realmuto, V. J., 2000: The potential use of earth observing system data to monitor the

964   passive emission of sulfur dioxide from volcanoes, In Remote Sens. of Active

965   Volcanism (Eds. P. Mouginis-Marks ,J. Crisp and J. Fink), Geophys. Monograph

966   116, AGU, Washington, 101−115.

967   Ross, J.K. and Marshak, A.L., 1988: Calculation of Canopy Bidirectional Reflectance

968   Using the Monte-Carlo Method. *Remote Sens. of Environment, 24*, 213-225.

969   Sassen, K., and S. Benson, 2001: A midlatitude cirrus cloud climatology from the facility

970   for atmospheric remote sensing. Part II: Microphysical properties derived from

971   lidar depolarization. *J. Atmos. Sci.,* **58**, 2103−2112.

972   Schmit, T. J., J. Li, J. J. Gurka, M. D. Goldberg, K. J. Schrab, J. Li, and W. F. Feltz,

973   2008: The GOES-R Advanced Baseline Imager and the continuation of current

974   sounder products. *J. Appl. Meteor.*, **47**, 2696−2711.

975   Schmit, T. J., P. Griffith, M. M. Gunshor, J. M. Daniels, S. J. Goodman, and W. J. Lebair,

976   2017: A closer look at the ABI on the GOES-R series. *Bulletin of the American*

977   *Meteorological Society*, **98**, 4, 681-698.

978   Stenberg, P., 1998: Implications of shoot structure on the rate of photosynthesis at

979   different levels in a coniferous canopy using a model incorporating grouping and

980   penumbra. *Functional Ecology,* 12, 82-91.

981   Stenberg, P., Mõttus, M., & Rautiainen, M., 2016: Photon recollision probability in

982   modelling the radiation regime of canopies — A review. *Remote Sensing of*

983   *Environ.,* 183, 98-108.

984   Stephens, G. L., S. C. Tsay, P. W. Stackhouse, Jr., and P. J. Flateau, 1990: The relevance

985   of the microphysical and radiative properties of cirrus clouds to the climate and

986   climatic feedback*, J. Atmos. Sci*. **47**, 1742–1753.

987   Torres O., P.K. Bhartia, J.R. Herman and Z. Ahmad, 1998: Derivation of aerosol

988   properties from satellite measurements of backscattered ultraviolet radiation.

989   Theoretical Basis, *J. Geophys. Res.*, 103, 17099-17110.

990   Torres, O., A. Tanskanen, B. Veihelman, C. Ahn, R. Braak, P. K. Bhartia, P. Veefkind,

991   and P. Levelt, Aerosols and Surface UV Products from OMI Observations: An

992   Overview, 2007: *J. Geophys. Res.,* 112, D24S47, doi:10.1029/2007JD008809.

993   Torres, O, H. Jethva, and P.K. Bhartia, 2012: Retrieval of Aerosol Optical Depth above

994   Clouds from OMI Observations: Sensitivity Analysis and Case Studies, *J. Atm.*

995   *Sci.*, 69, 1037-1053, doi:10.1175/JAS-D-11-0130.1.

996   Torres, O., C. Ahn, and Z. Chen, 2013: Improvements to the OMI near UV aerosol

997   algorithm using A-train CALIOP and AIRS observations, *Atmos. Meas. Tech.*, 6,

998   3257-3270, doi:10.5194/amt-6-3258-2013.

999   Tucker, C. J., 1979: Red and photographic infrared linear combination for monitoring

1000   vegetation, *Remote Sens. Environ.*, 8, 127-150.

1001   Wargan, K., Labow, G., Frith, S., Pawson, S., Livesey, N., and Partyka, G., 2017:

1002   Evaluation of the Ozone Fields in NASA's MERRA-2 Reanalysis. *J. Climate*, 30,

1003   2961-2988, https://doi.org/10.1175/JCLI-D-16-0699.1.

1004   Ustin, S.L., 2013: Remote sensing of canopy chemistry. *Proceedings of the National*

1005   *Academy of Sciences, 110*, 804-805.

1006   Wang, S., Grant, R., Verseghy, D., & Black, T., 2001: Modelling plant carbon and

1007   nitrogen dynamics of a boreal aspen forest in CLASS—the Canadian Land

1008   Surface Scheme. *Ecological Modelling, 142*, 135-154.

1009   Wargan, K., G. Labow, S. Frith, S. Pawson, N. Livesey, and G. Partyka, 2017: *J.*

1010   *Climate*, 30, DOI: http://dx.doi.org/10.1175/JCLI-D-16-0699.1.

1011   Wen, S., and Rose, W. I., 1994: Retrieval of particle sizes and masses in volcanic clouds

1012   using AVHRR bands 4 and 5*, J. Geophys. Res.*, 99, 5421-5431.

1013   Xu, X.*, J. Wang, Y. Wang, J. Zeng, O. Torres, Y. Yang, A. Marshak, J. Reid, and* S.

1014   Miller*,* 2017: Passive remote sensing of altitude and optical depth of dust plumes

1015   using the oxygen A and B bands: First results from EPIC/DSCOVR at Lagrange-1

1016   point*, Geophys. Res. Lett.,* 44*, doi:*10.1002/2017GL073939.

1017   Yang, B., Knyazikhin, Y., Mõttus, M., Rautiainen, M., Stenberg, P., Yan, L., Chen, C.,

1018   Yan, K., Choi, S., Park, T., & Myneni, R.B., 2017: Estimation of leaf area index

1019   and its sunlit portion from DSCOVR EPIC data: Theoretical basis. *Remote Sens.*

1020   *Environ.,* 198, 69-84.

1021 Yang, P., H.-L. Wei, B. A. Baum, H.-L. Huang, A. J. Heymsfield, Y. X. Hu, B.-C. Gao,

1022   and D. D. Turner, 2003: The spectral signature of mixed- phase clouds composed

1023   of nonspherical ice crystals and spherical liquid droplets in the terrestrial window

1024   region. *J. Quant. Spectrosc. Radiat. Transfer*, 79-80, 1171-1188.

1025 Yang, Y., A. Marshak, J. Mao, A. Lyapustin, J. Herman, 2013: A method of retrieving

1026   cloud top height and cloud geometrical thickness with oxygen A and B bands for

1027   the Deep Space Climate Observatory (DSCOVR) mission: Radiative transfer

1028   simulations. *J. Quant. Spectrosc. Radiat. Trans.* 122, 141-149, ISSN 0022-4073,

1029   http://dx.doi.org/10.1016/j.jqsrt.2012.09.017.

1030

1031 **Tables**

λ (nm) Center	FWHM (nm)	K_λ	S_λ (mW/m^2/nm)
317.5±0.1	1.0	1.216E-04	819.0
325.0±0.1	1.0	1.111E-04	807.7
340.0±0.3	2.7	1.975E-05	995.8
388.0±0.3	2.6	2.685E-05	1003.

1032

1033   **Table 1**. Calibration factors (K_λ) and irradiance at 1 AU (S_λ) for four UV channels.

1034

λ (nm) Center	FWHM (nm)	K_λ
443.0±1.0	2.6	8.340E-06
551.0±1.0	3.0	6.660E-06
680.0±0.2	1.6	9.300E-06
779.5±0.3	1.8	1.435E-05

1035

1036   **Table 2**. Calibration factors for three visible and one near-IR channel.

1037

λ (nm) Center	FWHM (nm)	K_λ
687.75±0.2	0.84	2.020E-05
764.0±0.2	1.02	2.360E-05

1038

1039   **Table 3**. Calibration factors for two O2-band channels.

1040

1041   **A list of the complete figure captions**

1042   **Figure 1.** Sun Earth View (SEV) angle (left axis, red curve) and the distance between DSCOVR and Earth

1043   (right axis, blue curve) are plotted versus the day since January 1, 2015. Note that SEV = 180° – scattering

1044   angle between solar and viewing directions. (SEV is usually stands for Sun Earth Vehicle where Vehicle

1045   refers to the Satellite).

1046   **Figure 2.** DSCOVR/EPIC 'enhanced' image of Africa (middle) taken on March 22, 2016 at 10:56 UTC.

1047   Left and right images show MODIS Terra and MODIS Aqua 2330 km wide swaths of the same area taken

1048   on the same day. Note that West Africa follows UTC time while East Africa is UTC plus 3 hours. Terra

1049   crosses equator at 10:30 am local time so that the western swath of the left image (Terra) resembles cloud

1050   structure on the left part of the EPIC image. Since Aqua crosses equator at 13:30 local time, the eastern

1051   Aqua swath part of the right (Aqua) and middle (EPIC) images are alike. Also note that the adjacent

1052   swaths of the MODIS examples are approximately 100 min apart.

1053   **Figure 3.** Schematic diagram of the geolocation process in Level 1A algorithm.

1054   **Figure 4.** Moon observations. Ratios of Moon reflectance F in counts/sec at 688 over 680 nm and at 764

1055   over 780 nm channels averaged over Moon pixels.

1056   **Figure 5.** EPIC retrieved ozone and LER values for April 21, 2016 at 16:58 UTC. The ozone scale is from

1057   100 to 500 DU, and the LER scale is from 0 to 100 percent.

1058   **Figure 6.** Left: EPIC ozone data compare to Pandora retrievals at Boulder Colorado. Right: daily (grey

1059   circles) and monthly (solid line) average difference between Pandora and EPIC ozone retrievals.

1060   **Figure 7.** Comparison of EPIC total column ozone with the MERRA-2 assimilation ozone model for April

1061   17, 2016.

1062   **Figure 8.** SO$_2$ maps for the March 2016 eruption of Pavlof volcano (AK, USA; triangle). SO$_2$ in the Pavlof

1063   volcanic ash cloud was detected in two EPIC exposures at (a) 21:54 UTC on March 28 and (b) 00:08 UTC

1064   on March 29; (c) Suomi-NPP/OMPS SO$_2$ measurements at ~23:25 UTC on March 28 produced using a

1065   Principal Component Analysis (PCA) SO$_2$ algorithm assuming a mid-tropospheric (TRM) volcanic plume

1066   located at 5-10 km altitude (Li et al., 2017); (d) Aqua/AIRS SO_2 measurements at ~23:29-23:35 UTC on

1067   March 28.

1068   **Figure 9.** EPIC derived UV aerosol index (top left), 388 nm aerosol optical depth (top right), 388 nm

1069   single scattering albedo (bottom left) and aerosol absorption optical depth (bottom right) derived from

1070   observations on August 7, 2016, 10:25 UTC.

1071   **Figure 10.** An example of EPIC data processing on 27 March 2016 at 1312 UTC: a) EPIC TOA RGB, b)

1072   atmospherically corrected RGB surface reflectance, 3) aerosol optical depth (AOD).

1073   **Figure 11.** Sample EPIC L2 cloud products for the observations at 14:57 UTC on June 23, 2016: (a) EPIC

1074   RGB image; (b) EPIC cloud mask. 1: high confidence clear, 2: low confidence clear, 3: low confidence

1075   cloudy, and 4: high confidence cloudy; (c) oxygen A-band cloud effective pressure; (d) cloud optical

1076   thickness assuming liquid phase; (e) cloud optical thickness assuming ice phase; (f) most likely cloud

1077   phase. Other L2 cloud products not shown include oxygen B-band cloud effective pressure, and A- and B-

1078   band cloud effective height.

1079   **Figure 12.** NDVI, FPAR and SLAI on Aug-23-2016 at 15:24:58 UTC. Corresponding EPIC image of the

1080   sunlit Earth is shown in Fig. 13.

1081   **Figure 13.** Left panel: enhanced RGB image of the sunlit face of the Earth

1082   (http://epic.gsfc.nasa.gov/enhanced) taken on Aug-23-2016 at 15:24:58 UTC. Left panel: NIR BRF of an

1083   area in Amazonian rain forest shown as red circle derived from MISR data (symbols) and EPIC (white

1084   square). Horizontal axis shows values of the phase angle, i.e., the angle between directions to the Sun and

1085   sensor.

1086   **Figure 14.** Vegetation dynamics. False color image (688-551-680) of the scattering coefficient derived

1087   from DSCOVR EPIC images taken on Feb-11-2016 at 13:22 UTC and Aug-23-2016 at 13:14 UTC using a

1088   simple algorithm documented in (Marshak & Knyazikhin, 2017). The green color indicates green leaves

1089   that EPIC sees through the atmosphere. The images capture changes in savannas from wet (approximately

1090   June to September) and dry (October to May) seasons when area of green leaves increases during the wet

1091   season and decreases during the dry season.

1092 **Figure 15**. *MODIS and EPIC NDVIs.* The left panel shows MODIS/Terra surface NDVI composited over

1093 March, 2016 (https://giovanni.gsfc.nasa.gov/giovanni/). The middle and the right panels are EPIC NDVIs

1094 for March 22, 2016 (10:52 UTC) calculated with the red and O2 B-band channels, respectively. The insert

1095 in the right panel is the RGB plot. The use of the O2 B-band enhances the sensitivity of the TOA NDVI to

1096 the presence of vegetation. Note that EPIC data do not have any atmospheric correction nor cloud mask.

1097 Areas with high MODIS NDVI and very small EPIC NDVI are likely covered by clouds. From Marshak

1098 and Knyazikhin (2017).

1099 **Figure 16**. *An example of terrestrial glint.* A true-color composite image captured on Oct. 28, 2015 at 9:46

1100 UTC is shown (all EPIC true-color images are available at http://epic.gsfc.nasa.gov). The pixel size is

1101 about 10x10 km^2 and angular spread ~3×10^{-4} degree. A wheel inside EPIC spins color filters, causing a

1102 time lag between the component images: ~3 min between blue (443 nm) and green (551 nm), ~4 min

1103 between blue and red (680 nm), resulting in a coloration effect in the imagery. The framed region contains

1104 a bright colorful spot discernible by a naked eye and centered at 8.31° S and 25.5° E (magnified in the

1105 inset).

1106 **Figure 17**. *Erythemal irradiance.* (a) April 1, 2016 over Central and South America. (b) November 27,

1107 2016 over South America.

1108

1109

1110 **Figures**

Legend: SEV_angle[deg] — Earth_sat_dist[km]

Y-axis (left): SEV_angle[deg], 4 to 12
Y-axis (right): Earth_sat_dist[km], 1.35 10⁶ to 1.6 10⁶

Annotations in plot:
163=June 12, 2015
366=Jan 1, 2016
487=May 1, 2016
610=Sep 1, 2016
732=Jan 1, 2017
822=April 1, 2017
913=July 1, 2017
1036=Nov 1, 2017

X-axis: DAY (since 01/01/2015), 200 to 1200

1111

1112

1113 **Figure 1.** Sun Earth View (SEV) angle (left axis, red curve) and the distance between DSCOVR and Earth

1114 (right axis, blue curve) are plotted versus the day since January 1, 2015. Note that SEV = 180° – scattering

1115 angle between solar and viewing directions. (SEV is usually stands for Sun Earth Vehicle where Vehicle

1116 refers to the Satellite).

1117
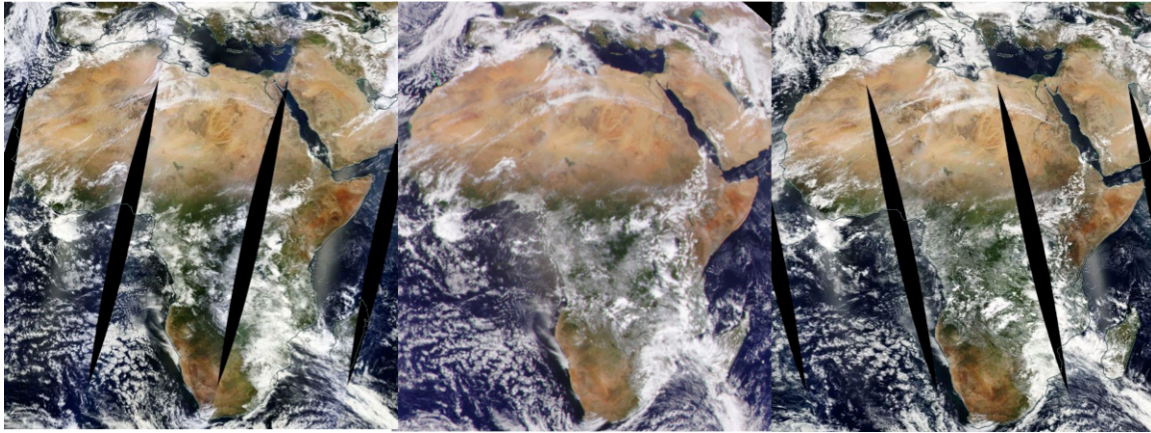
1118

1119   MODIS Terra   EPIC 10:56 GMT   MODIS Aqua

1120 10:30 equatorial crossing time   13:30 equatorial crossing time

1121

1122 **Figure 2.** DSCOVR/EPIC 'enhanced' image of Africa (middle) taken on March 22, 2016 at 10:56 UTC.

1123 Left and right images show MODIS Terra and MODIS Aqua 2330 km wide swaths of the same area taken

1124 on the same day. Note that West Africa follows UTC time while East Africa is UTC plus 3 hours. Terra

1125 crosses equator at 10:30 am local time so that the western swath of the left image (Terra) resembles cloud

1126 structure on the left part of the EPIC image. Since Aqua crosses equator at 13:30 local time, the eastern

1127 Aqua swath part of the right (Aqua) and middle (EPIC) images are alike. Also note that the adjacent

1128 swaths of the MODIS examples are approximately 100 min apart.

1129
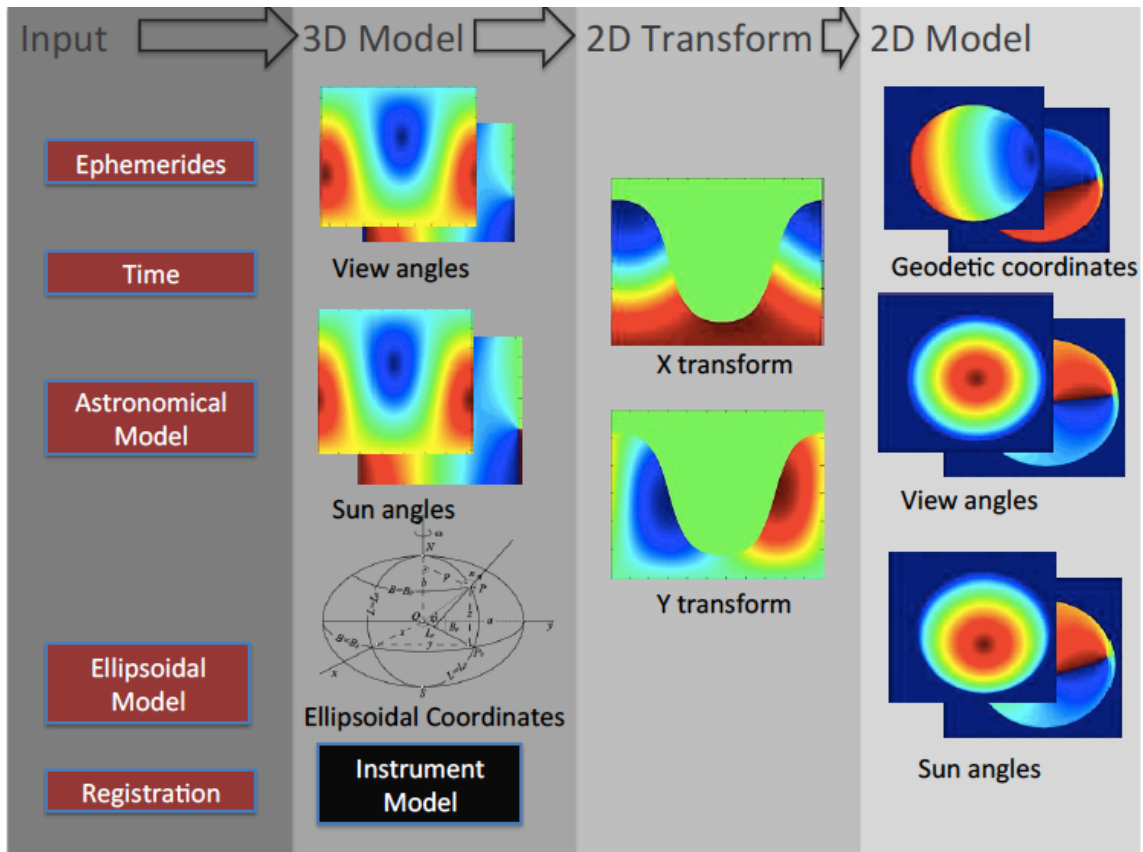
1130

1131 **Figure 3.** Schematic diagram of the geolocation process in Level 1A algorithm.

1132

1133

Figure 4. Moon observations. Ratios of Moon reflectance *F* in counts/sec at 688 over 680 nm and at 764

1135   over 780 nm channels averaged over Moon pixels.

1136
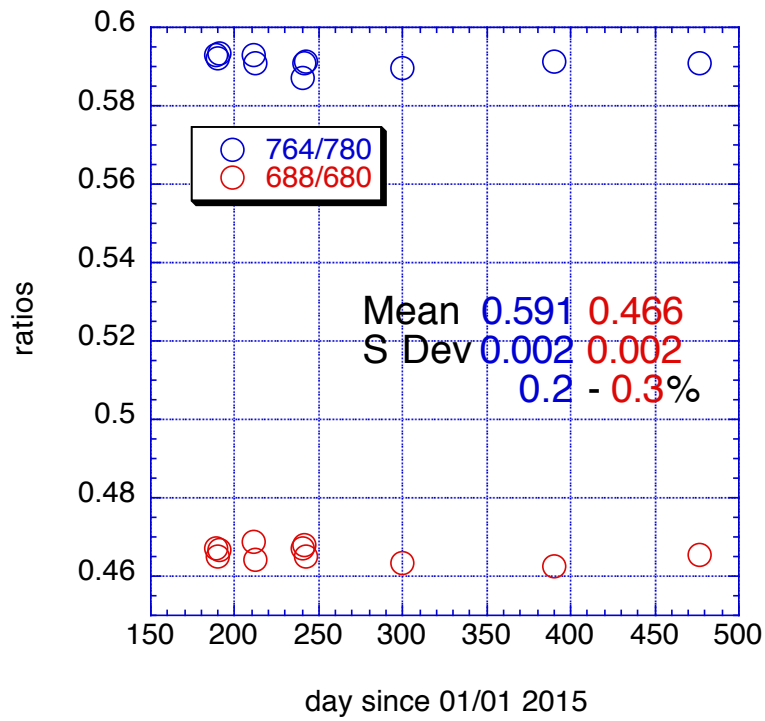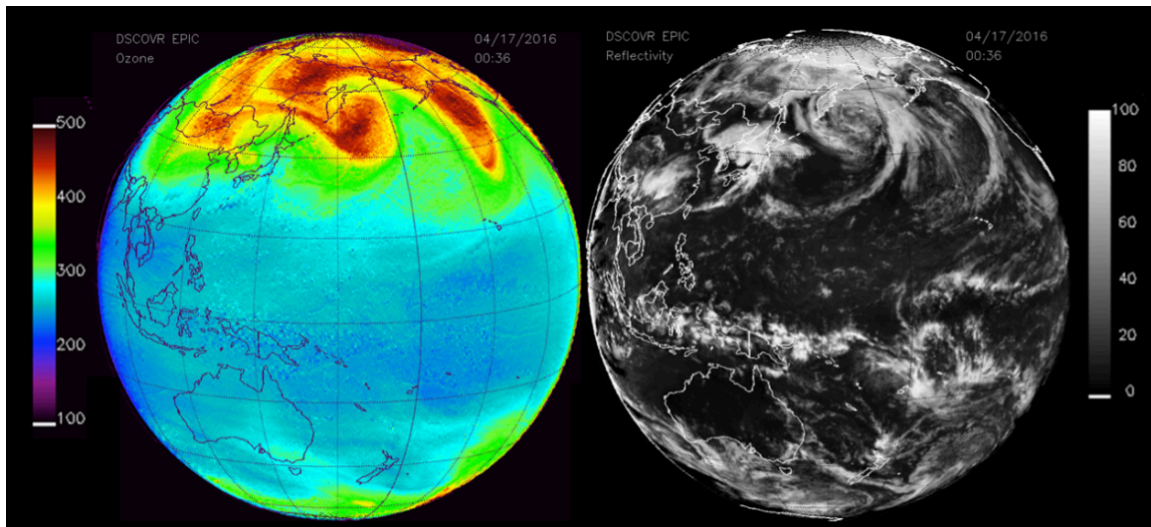
Figure 5. EPIC retrieved ozone and LER values for April 21, 2016 at 16:58 UTC. The ozone scale is from 100 to 500 DU, and the LER scale is from 0 to 100 percent.
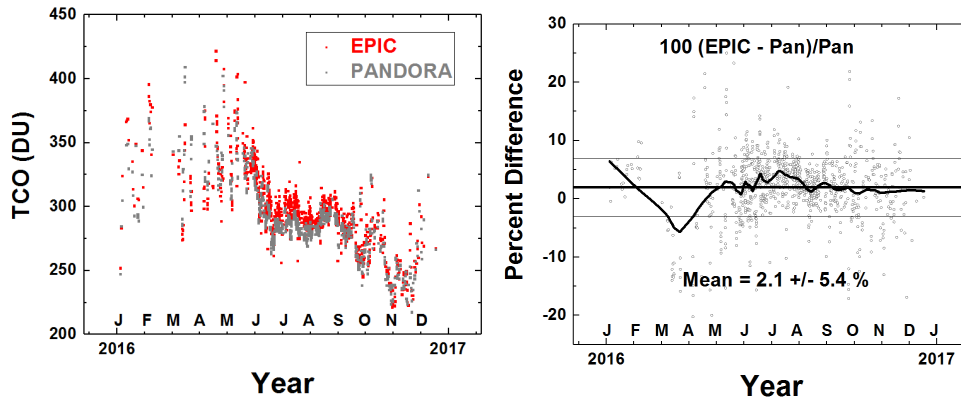
1141

1142 **Figure 6.** Left: EPIC ozone data compare to Pandora retrievals at Boulder Colorado. Right: daily (grey

1143 circles) and monthly (solid line) average difference between Pandora and EPIC ozone retrievals.

1144

EPIC Total Ozone   MERRA-2 Total Ozone

17 April 2016   18:35 GMT
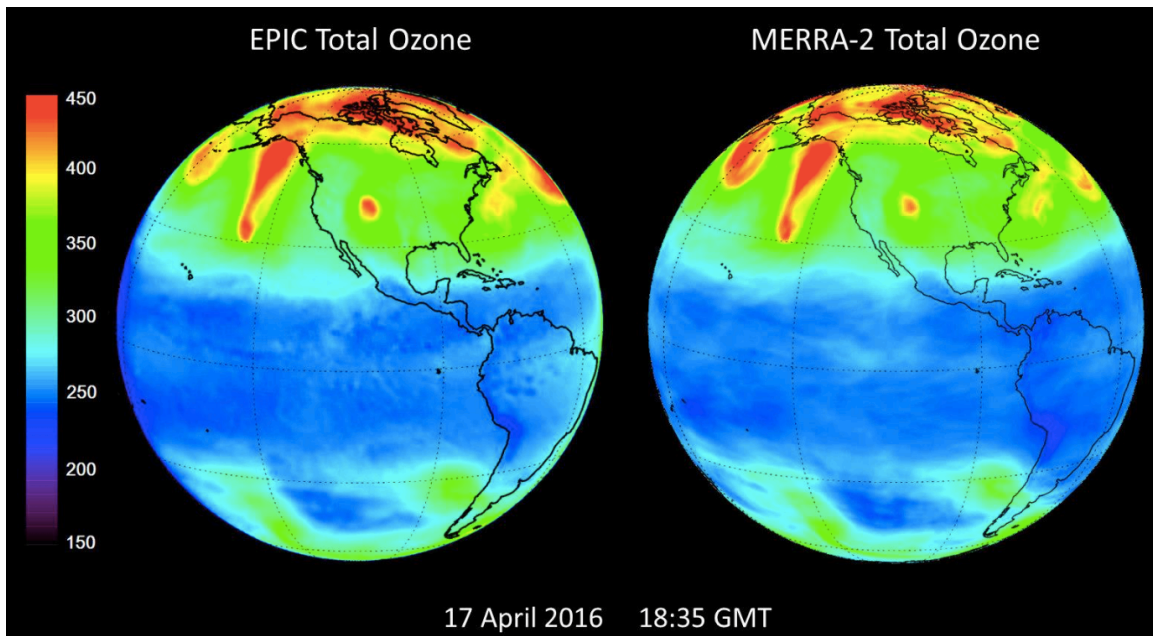
Figure 7. Comparison of EPIC total column ozone with the MERRA-2 assimilation ozone model for April 17, 2016.
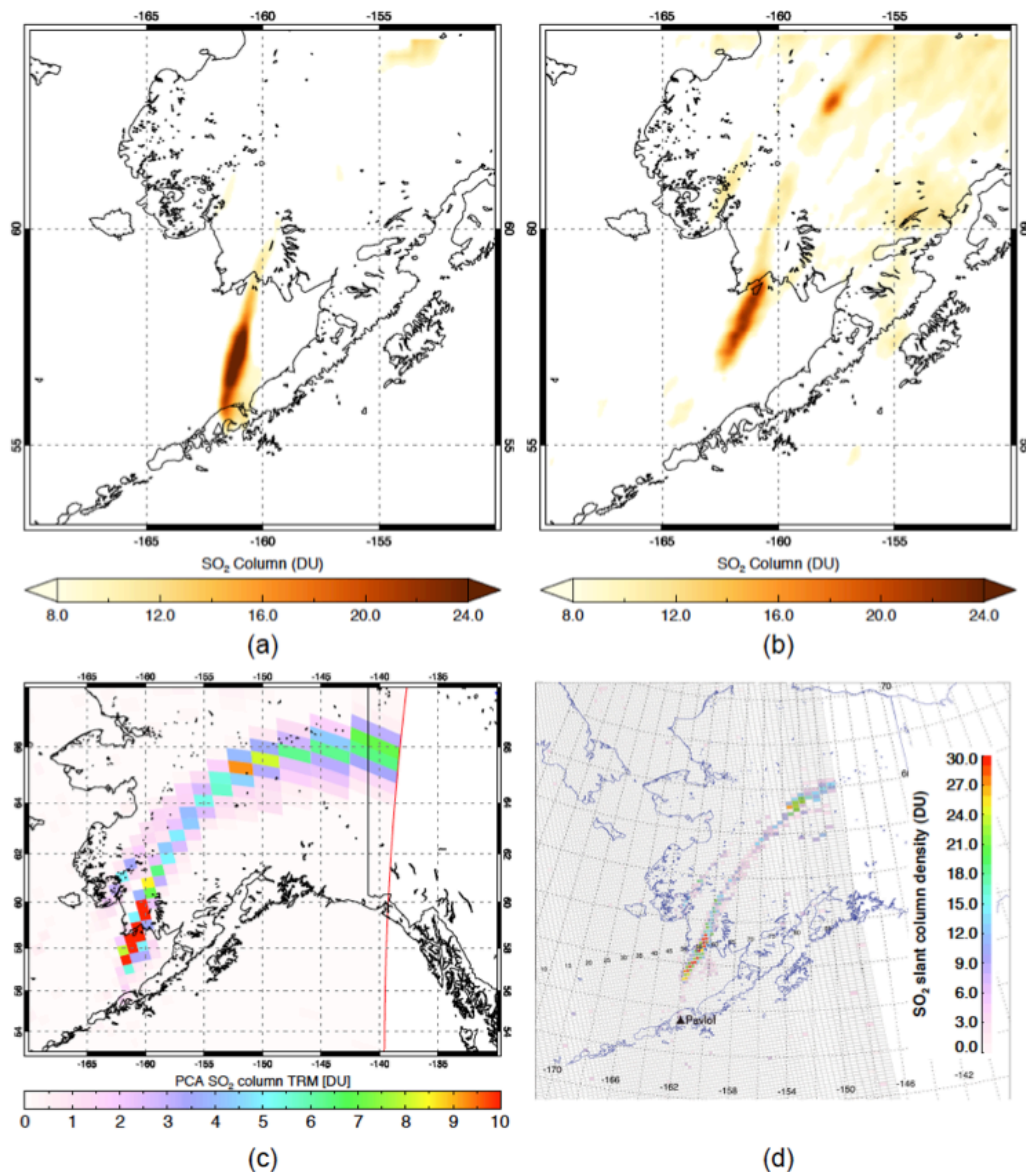
Figure 8. SO$_2$ maps for the March 2016 eruption of Pavlof volcano (AK, USA; triangle). SO$_2$ in the Pavlof volcanic ash cloud was detected in two EPIC exposures at (a) 21:54 UTC on March 28 and (b) 00:08 UTC on March 29; (c) Suomi-NPP/OMPS SO$_2$ measurements at ~23:25 UTC on March 28 produced using a Principal Component Analysis (PCA) SO$_2$ algorithm assuming a mid-tropospheric (TRM) volcanic plume located at 5-10 km altitude (Li et al., 2017); (d) Aqua/AIRS SO$_2$ measurements at ~23:29-23:35 UTC on March 28.
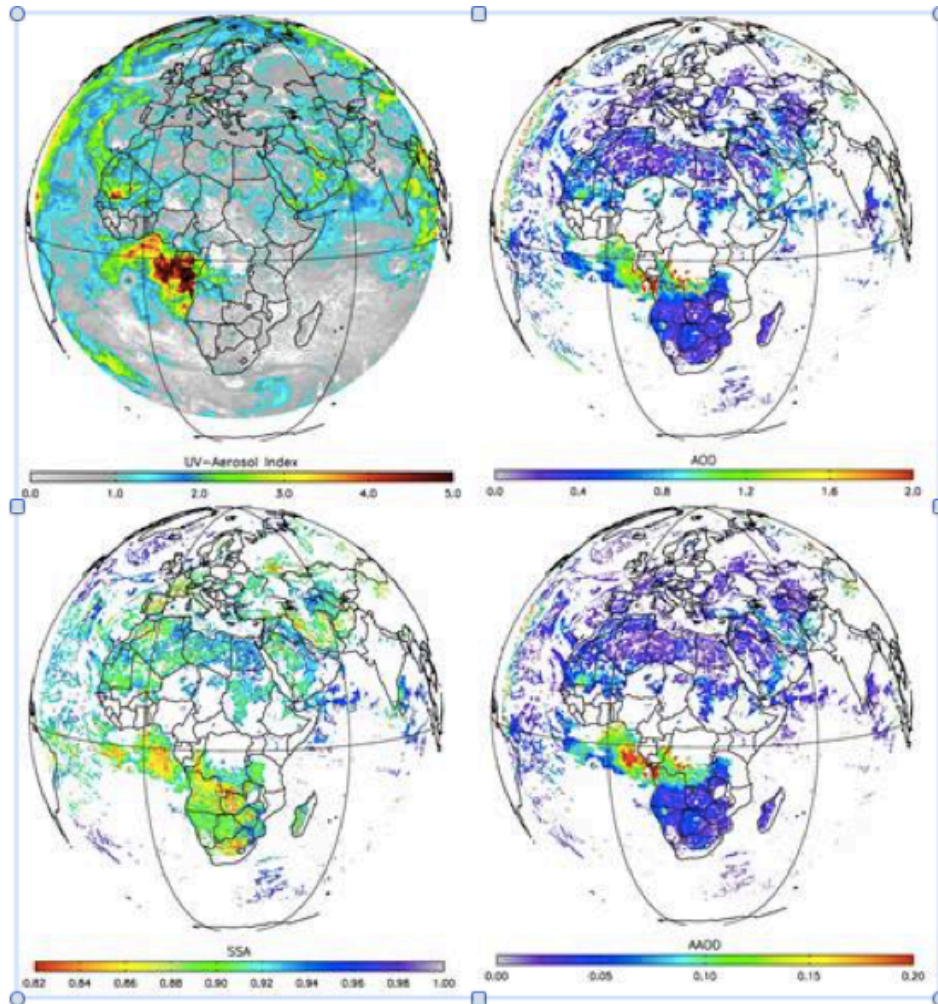
1156

Figure 9. EPIC derived UV aerosol index (top left), 388 nm aerosol optical depth (top right), 388 nm single scattering albedo (bottom left) and aerosol absorption optical depth (bottom right) derived from observations on August 7, 2016, 10:25 UTC.
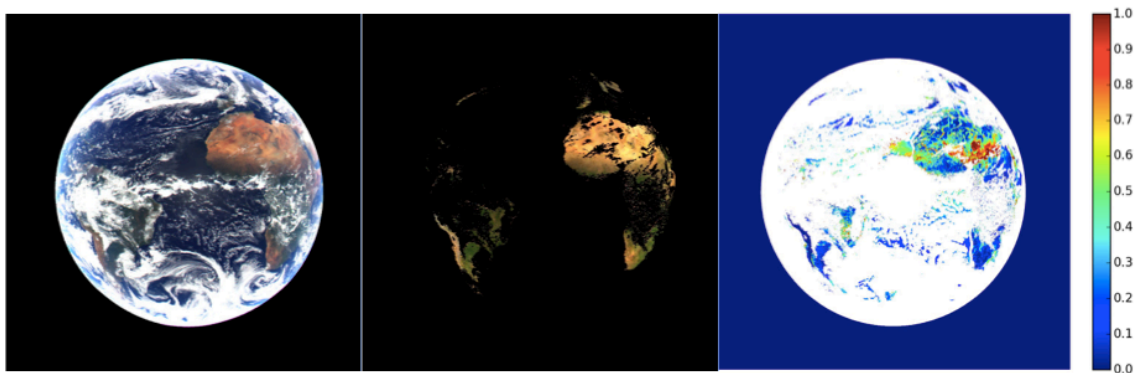
1157
1158
1159

1160

1161

1162 **Figure 10.** An example of EPIC data processing on 27 March 2016 at 1312 UTC: a) EPIC TOA RGB, b)

1163 atmospherically corrected RGB surface reflectance, 3) aerosol optical depth (AOD).

1164
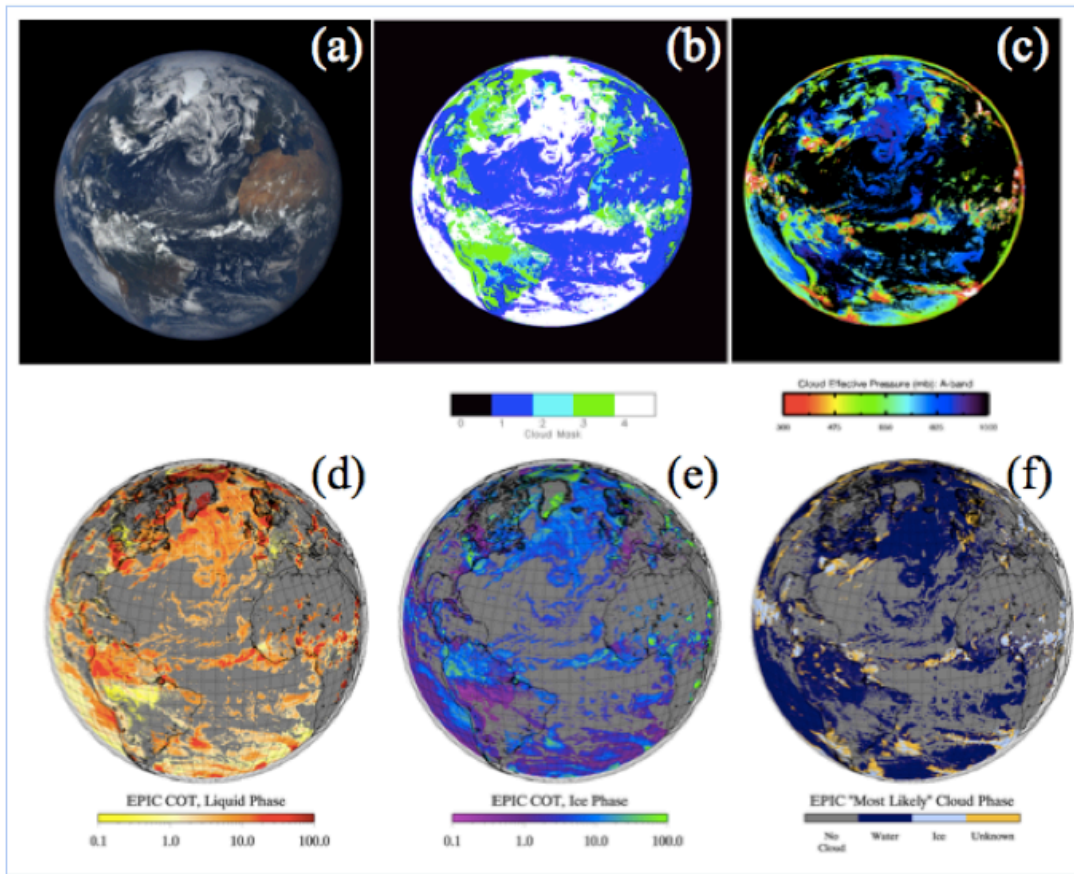
Figure 11. Sample EPIC L2 cloud products for the observations at 14:57 UTC on June 23, 2016: (a) EPIC RGB image; (b) EPIC cloud mask. 1: high confidence clear, 2: low confidence clear, 3: low confidence cloudy, and 4: high confidence cloudy; (c) oxygen A-band cloud effective pressure; (d) cloud optical thickness assuming liquid phase; (e) cloud optical thickness assuming ice phase; (f) most likely cloud phase. Other L2 cloud products not shown include oxygen B-band cloud effective pressure, and A- and B-band cloud effective height.
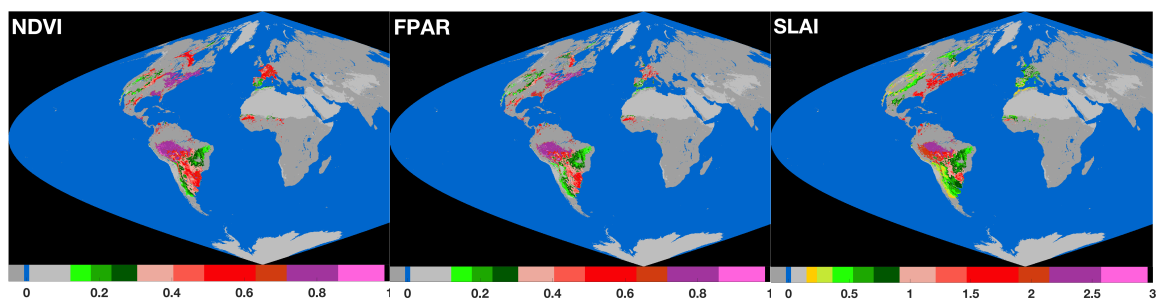
1173

1174

1175 **Figure 12.** NDVI, FPAR and SLAI on Aug-23-2016 at 15:24:58 UTC. Corresponding EPIC image of the

1176 sunlit Earth is shown in Fig. 13.

1177

1178
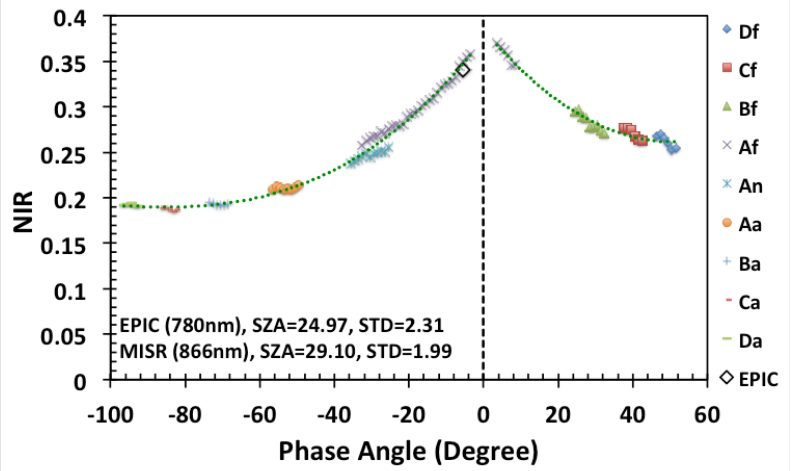
1179

1180 **Figure 13.** Left panel: enhanced RGB image of the sunlit face of the Earth

1181 (http://epic.gsfc.nasa.gov/enhanced) taken on Aug-23-2016 at 15:24:58 UTC. Left panel: NIR BRF of an

1182 area in Amazonian rain forest shown as red circle derived from MISR data (symbols) and EPIC (white

1183 square). Horizontal axis shows values of the phase angle, i.e., the angle between directions to the Sun and

1184 sensor.

1185
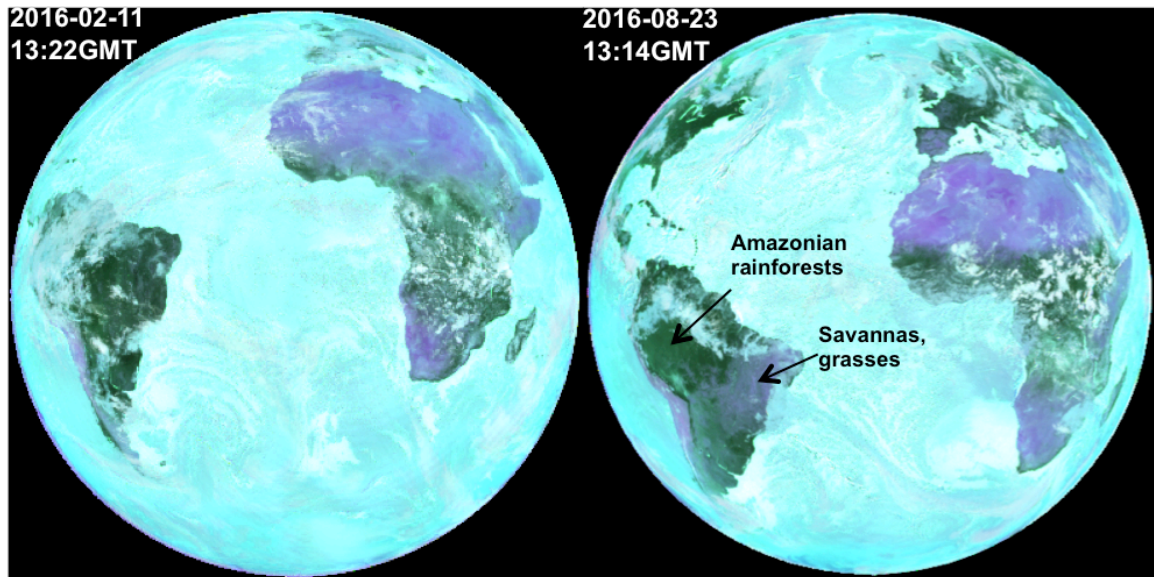
2016-02-11
13:22GMT

2016-08-23
13:14GMT

Amazonian
rainforests

Savannas,
grasses

1186

Figure 14. Vegetation dynamics. False color image (688-551-680) of the scattering coefficient derived

1187

1188   from DSCOVR EPIC images taken on Feb-11-2016 at 13:22 UTC and Aug-23-2016 at 13:14 UTC using a

1189   simple algorithm documented in (Marshak and Knyazikhin, 2017). The green color indicates green leaves

1190   that EPIC sees through the atmosphere. The images capture changes in savannas from wet (approximately

1191   June to September) and dry (October to May) seasons when area of green leaves increases during the wet

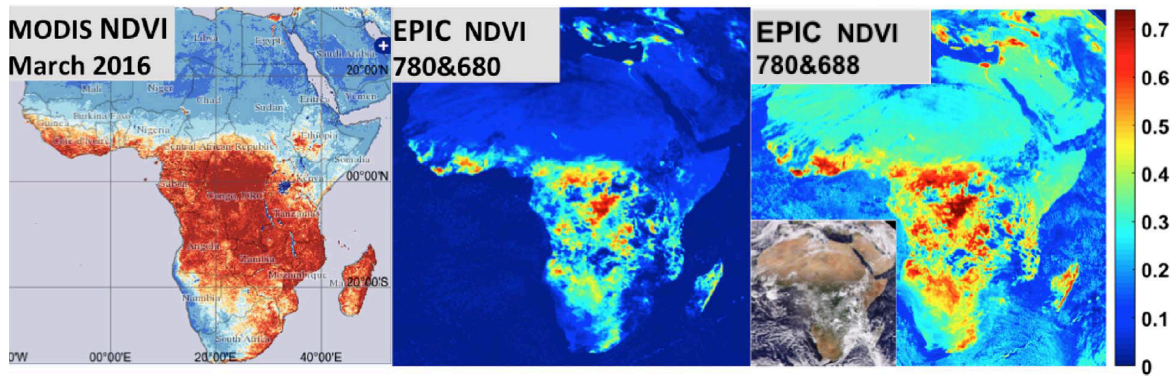1192   season and decreases during the dry season.

1193

Figure 15. *MODIS and EPIC NDVIs.* The left panel shows MODIS/Terra surface NDVI composited over March, 2016 (https://giovanni.gsfc.nasa.gov/giovanni/). The middle and the right panels are EPIC NDVIs for March 22, 2016 (10:52 UTC) calculated with the red and O2 B-band channels, respectively. The insert in the right panel is the RGB plot. The use of the O2 B-band enhances the sensitivity of the TOA NDVI to the presence of vegetation. Note that EPIC data do not have any atmospheric correction nor cloud mask. Areas with high MODIS NDVI and very small EPIC NDVI are likely covered by clouds. From Marshak and Knyazikhin (2017).
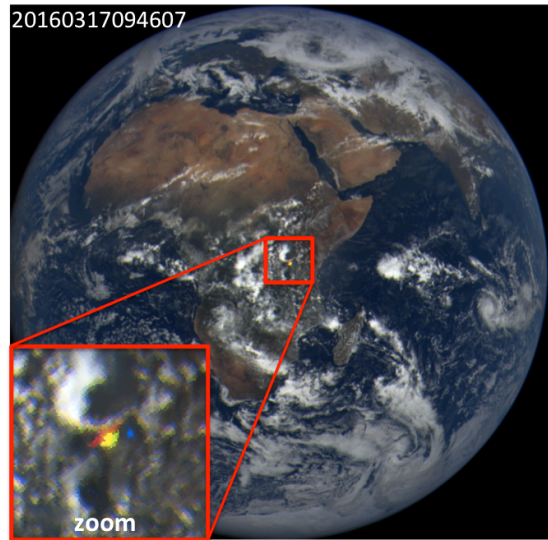
Figure 16. *An example of terrestrial glint.* A true-color composite image captured on Oct. 28, 2015 at 9:46

UTC is shown (all EPIC true-color images are available at http://epic.gsfc.nasa.gov). The pixel size is

about 10x10 km^2 and angular spread ~3x10^{-4} degree. A wheel inside EPIC spins color filters, causing a

time lag between the component images: ~3 min between blue (443 nm) and green (551 nm), ~4 min

between blue and red (680 nm), resulting in a coloration effect in the imagery. The framed region contains

a bright colorful spot discernible by a naked eye and centered at 8.31° S and 25.5° E (magnified in the
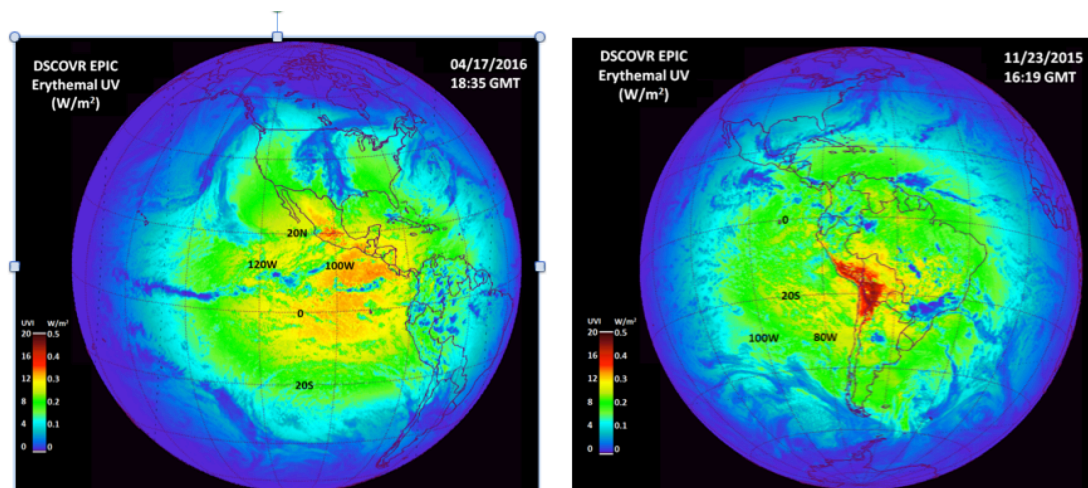
inset).

Figure 17. *Erythemal irradiance.* (a) April 1, 2016 over Central and South America. (b) November 27, 2016 over South America.